MOLECULAR DISSECTION OF BSC2: A NOVEL NEGATIVE REGULATOR OF TRIGLYCERIDE LIPOLYSIS FOR A LIPID DROPLET SUBPOPULATION

APPROVED BY SUPERVISORY COMMITTEE

Mike Henne, Ph.D. (Supervisor)

Joel Goodman, Ph.D. (Chair)

Daniela Nicastro, Ph.D.

Jonathan Friedman, Ph.D.

DEDICATION

I would like to thank my husband and love of my life Andrew Speer, my daughter Noelle Speer, my best friend Loren Rose, and my mentor Mike Henne

MOLECULAR DISSECTION OF BSC2: A NOVEL NEGATIVE REGULATOR OF TRIGLYCERIDE LIPOLYSIS FOR A LIPID DROPLET SUBPOPULATION

by

NATALIE ORTIZ SPEER

DISSERTATION

Presented to the Faculty of the Graduate School of Biomedical Sciences

The University of Texas Southwestern Medical Center at Dallas

In Partial Fulfillment of the Requirements

For the Degree of

DOCTOR OF PHILOSOPHY

The University of Texas Southwestern Medical Center at Dallas

Dallas, Texas

December, 2023

MOLECULAR DISSECTION OF BSC2: A NOVEL NEGATIVE REGULATOR OF TRIGLYCERIDE LIPOLYSIS FOR A LIPID DROPLET SUBPOPULATION

Natalie Ortiz Speer

The University of Texas Southwestern Medical Center at Dallas, 2023

Supervising Professor: W. Mike Henne, Ph.D.

Eukaryotic cells store lipids in the form of triglyceride (TG) and sterol-ester (SE) in cytoplasmic organelles called lipid droplets (LDs). Distinct pools of LDs with unique surface proteomes exist in cells, but a pervasive question is how proteins localize to and convey functions to specific LD subsets. Here, we show the yeast protein Bsc2 localizes to a specific subset of TG-containing LDs, and reveal it negatively regulates TG lipolysis. Mechanistically, Bsc2 LD targeting requires TG, and LD targeting is mediated by specific N-terminal hydrophobic regions (HRs) sufficient for Bsc2 function. Molecular dynamics simulations reveal these Bsc2 HRs interact extensively with TG on modeled LDs, and adopt a specific conformation on TG-rich LDs versus SE-rich LDs or a modeled ER bilayer. Bsc2-deficient yeast display no defect in LD biogenesis, but exhibit enhanced TG lipolysis dependent on the

major TG lipase Tgl3. Remarkably, over-expression of Bsc2, but not LD protein Pln1, causes TG accumulation without altering SE levels. Finally, we find that Bsc2-deficient cells display altered LD accumulation during stationary phase growth. We propose that Bsc2 is a novel regulator of TG lipolysis that localizes to a subset of TG-enriched LDs and locally regulates TG lipolysis.

ACKNOWLEDGEMENTS

The number of people I could thank for supporting me during my graduate school journey could honestly fill the pages of this dissertation, but I will try my best to not get carried away.

First, I'd like thank my mentor and jedi master, Mike Henne. I distinctly remember back in 2016, prior to graduate school, while still working as a technician in the Goodman Lab, I sat in on my first ION Club meeting hosted by the Henne Lab. There, I saw how truly supportive Mike is of his trainees, and felt how infectious his love for cell biology is (in particular, the yeast NVJ, but probably now, lipid droplets). Once I started graduate school here at UT Southwestern in Summer of 2017, I knew I wanted to rotate in Mike's lab, and secured a spot for my second rotation. Halfway through, I knew the Henne Lab was the perfect environment for me to train as scientist. I loved how Mike had fostered such a kind and supportive environment. In particular, Mike's open door policy and communicative mentorship style was instrumental in my deciding to join the lab in October 2017. Flash forward 6 years and I couldn't be more thankful I became a fully fledged member of the Henne Lab. Anytime I've felt dejected about my project, or am trying to figure out why my cloning isn't working, or am just simply stressed about grad school in general, I can pop into Mike's office to chat and come out feeling a thousand times more refreshed about the situation. Mike is a natural born leader and gifted mentor, who's motivation and confidence is truly contagious. In particular, I want to thank Mike from the bottom of my heart for his patience, kindness, and understanding in the face of the many personal challenges I've weathered throughout graduate

school. I'm sorry for all the times I've cried in Mike's office (we could probably build a small aquarium), but I am forever grateful he gave me the freedom to be vulnerable and human.

I'd also like to extend a huge thanks to past and present members of the Henne Lab for their constant support and friendship over the years: Hanaa Hariri, Sanchari Datta, Sean Rogers, Jade Bowerman, Anastasia Kovalenko, Rupali Ugrankar, Blessy Paul, Emma Reynolds, Holly Merta, Chetana Jadhav, Kaitlynn Gov, Son Tran, and Alicja Brudnicka. Every one of you has made a significant and distinctly positive impact on me during my time as a student and for that I am so grateful. In particular, I'd like to thank Hanaa Hariri, who I worked under during my Henne lab rotation and since then, we have developed a wonderful bond and friendship over the years. Hanaa was (and is) a constant source of support and motivation, as well as a wonderful role model for women in science everywhere. Her guidance has been instrusmental in my success in grad school. I also want to thank Sanchari for being such a great labmate and friend. Sanchari's advice and general chats helped me get through many late nights in lab. I want to thank Sean for always taking the time to answer my mundane questions, offer feedback, and for kindly offering his skillfully troubleshot protocols. I'd like to give another huge thank you to Rupali and Blessy for being such great sources of support and advice, inside and out of lab, especially during my pregnancy and after I became a mother. Lastly, I'd like to thank our brilliant, talented, and kind technician, Emma Reynolds. Without her dedicated work ethic and skillset, none of this project, especially the mammalian cell culture work, would have been possible. I especially want to thank Emma for being my lab confidant. All those hours purifying protein together blossomed into a wonderful friendship and I am honored to call her my colleague.

I would also like to thank the members of my thesis committee: Joel Goodman, Jonathan Friedman, and Daniela Nicastro. All three have brought unique and enriching perspectives to the table when discussing my thesis project at committee meetings. Their constructive advice and feedback truly changed the trajectory of my project and I owe a major part of the success of this project to them. I would also like to thank my committee members for their incredible kindness, patience, and support during my times of personal struggle over the years in grad school. I'd like to also extend another huge thank you to Joel Goodman. When Joel hired me as his lab technician back in May 2016, I was ecstatic. Under Joel's mentorship, I developed a true love for metabolism and cell biology, despite that I was a trained microbiologist. Joel's passion for studying droplet metabolism, paired with his infectiously positive personality reinvigorated my appeal for academia. Had it not been for Joel's encouragement and support during the graduate school application process, I don't believe I would be where I am today. I am wholly grateful to Joel for his significant role in my graduate school success.

I also want to thank my Dallas friends: Loren Rose, Christy Carry, Chelsea Lousignont, Katrina Connor, and Danielle Burns. I would not have survived the stresses of graduate school had it not been for these ladies, as they helped me put life into perspective with a laugh and a good meal. In particular, I want to thank my best friend, my Tina Belcher, Loren Rose. Loren has been my ultimate cheerleader and confidant during my time as a PhD student. She was always ready to share in my successes, while also commiserating with me in my failures (which includes making me laugh with ridicious memes). I am eternally grateful to have Loren in my life.

Lastly, I'd like to thank my husband, Andrew Speer. Words cannot describe how much Andrew's love and support has meant to me over the years, but in particular during my time in graduate school. From proof-reading my graduate school applications, to helping me practice my work-in-progress talks, to watching our infant daughter while I attended ASCB in Washington D.C., Andrew has been instrumental in my success as a PhD student and scientist. During my time at UTSW, Andrew and I got engaged, got married, bought a house, and had a baby (just to name a few)! In the midst of the highs and lows of my career as a scientist and in my personal life, Andrew has celebrated with me in the victories, and been strong for me when I couldn't be during the painful losses. Andrew is not just my husband, but my best friend and an amazing father to our beautiful daughter Noelle. Grad school has been exceptionally tough, but coming home to my husband and daughter has, and continues to bring me a tremendous amount of love, happiness, and purpose.

TABLE OF CONTENTS

PREFACE v

ACKNOWLEDGEMENTS vii

TABLE OF CONTENTS xi

PRIOR PUBLICATIONS xiv

LIST OF FIGURES xv

LIST OF SUPLEMENTARY FIGURES xvi

LIST OF APPENDICES xvii

LIST OF DEFINITIONS xviii

CHAPTER ONE INTRODUCTION 1

Background 1

Neutral lipid synthesis and lipid droplet (LD) biogenesis 3

LD protein targeting 6

LD turnover via lipolysis 8

Hypothesis 9

CHAPTER TWO BSC2 IS A NOVEL REGULATOR OF TRIGLYCERIDE LIPOLYSIS THAT DEMARCATES A LIPID DROPLET SUBPOPULATION 12

Abstract 12

Introduction 12

Results 15

Bsc2 localizes to a LD subset and requires TG for targeting 15

The Bsc2 N-terminal hydrophobic regions mediate LD targeting 18

Molecular dynamics simulations suggest Bsc2 HRs adopt specific conformations on TG-rich LDs 22

Loss of Bsc2 alters TG levels via enhanced TG lipolysis 30
The Bsc2 HR1 and HR2 regions are sufficient for Bsc2 function 32
Bsc2 over-expression results in TG and LD enlargement 36
Bsc2 loss or over-expression does not impact Tgl lipase abundance nor LD targeting 39
Bsc2 and Tgl3 independently target to LD subsets 40
Bsc2 loss alters LD accumulation in yeast stationary phase 44
Discussion 46

CHAPTER THREE MATERIALS AND METHODS 49
Yeast strains and growth conditions 49
Molecular dynamics simulations 51
Structure prediction 51
Simulations 51
Metadynamics 53
Lipid extraction and TLC 53
TLC quantification 54
LD number and area quantification 55
Fluorescent signal quantification of Bsc2 and Tgl3 imaging under cerulenin treatment 55
Statistical analysis 56
Conventional TEM 56
Whole cell protein extraction and sample preparation 56
Immunoblot analysis 57
Whole cell protein extraction for immunoprecipitation 58
Immunoprecipitation (IP) 59
LC-MS/MS proteomics 60
Cell culture 61
Cloning and transient transfection 62

IF staining 62
Fluorescence microscopy 63
Yeast strain generation and plasmid construction 63
Proteomics quantification 64
Cartoon development 65

CHAPTER FOUR DISCUSSION AND FUTURE DIRECTIONS 67
Significance 67
Future directions 68
In closing 70

PRIOR PUBLICATIONS

Speer, N.O., Braun, R.J., Reynolds, E.G., Swanson, M.J., Henne, W.M. Bsc2 is a novel regulator of triglyceride lipolysis that demarcates a lipid droplet subpopulation. *BioRxiv*.

Rogers, S., Gui, L., Kovalenko, A., Zoni, V., Carpentier, M., Ramji, K., Mbarek, K.B., Bacle, A., Fuchs, P., Campomanes, P., Reetz, E., Speer, N.O., Reynolds, E., Thiam, A.R., Vanni, S., Nicastro, D., Henne, W.M. (2022). Triglyceride lipolysis driven by glucose restriction triggers liquid-crystalline phase transitions and proteome remodeling of lipid droplets. *Journal of Cell Biology*. Nov 7; 221(11):e202205053

Gok, M.O., Speer, N.O., Henne, W.M., Friedman, J.R. (2022). ER-localized phosphatidylethanolamine synthase plays a conserved role in lipid droplet formation. *Molecular Biology of the Cell*. Jan 1; 33:ar11, 1-12

Rogers, S., Hariri, H., Wood , N.E., Speer, N.O., Henne, W.M. (2021). Glucose restriction drives spatial reorganization of mevalonate metabolism. *eLife*. Apr 7; 10:e62591

Hariri, H., Speer, N.O., Bowerman, J., Rogers S., Fu, G., Reetz, E., Datta, S., Feathers, J.R., Ugrankar, R., Nicastro, D., Henne, W.M. (2019). Mdm1 maintains endoplasmic reticulum homeostasis by spatially regulating fatty acid processing and lipid droplet biogenesis. *Journal of Cell Biology*. Apr 1; 218(4): 1319-1334

Gao, Q., Binns, D.D., Kinch, L.N., Grishin, N.V., Ortiz, N., Chen, X., and Goodman, J.M. (2017). Pet10p is a yeast perilipin that stabilizes lipid droplets and promotes their assembly. *Journal of Cell Biology*. Oct 2; 216(10):3199-3217

LIST OF FIGURES

Figure 2.1 Bsc2 enriches on a TG-containing LD subpopulation 17
Figure 2.2 Hydrophobic Region 1 (HR1) of Bsc2 is responsible for LD-targeting 21
Figure 2.3 Molecular dynamics simulations indicate Bsc2 adopts a unique conformational ensemble on TG-rich LDs 27
Figure 2.4 Bsc2 deletion results in enhanced Tgl3 lipase-dependent TG lipolysis 34
Figure 2.5 Overexpression of Bsc2 signficantly elevates TG levels, LD number, and LD size 38
Figure 2.6 Bsc2 does not alter TG lipase LD-targeting or protein abundance, but modulates lipolysis on the LD 43
Figure 2.7 Bsc2 influences LD maintenance during late starvation conditions 45

LIST OF SUPPLEMENTARY FIGURES

Supplementary Figure 2.3 MD analysis of Bsc2 HR1 and HR2 conformations 29

LIST OF APPENDICES

APPENDIX A Table of Yeast Strains 72

APPENDIX B Table of Plasmids 74

LIST OF DEFINITIONS

LD	Lipid Droplet
TG	Triglyceride/Triacylglycerol
SE	Sterol Ester
ER	Endoplasmic Reticulum
FA	Fatty Acid
NL	Neutral Lipid
AH	Amphipathic Helix
MD	Molecular Dynamics
WT	Wild Type
CHYO	Cholesteryl Oleate
TEM	Transmission Electron Microscopy
mNG	mNeonGreen
GGR	Gradual Glucose Restriction
LOG	Logarithmic
STAT	Stationary
PL	Phospholipid
MDH	Monodansylpentane
HR1	Hydrophobic Region 1
HR2	Hydrophobic Region 2
LCR	Low Complexity Region
OA	Oleic Acid/Oleate
LC-MS/MS	Liquid Chromatography Mass Spectrometry
OE	Over-expression
IP	Immunoprecipitation
TLC	Thin Layer Chromatography
EV	Empty Vector
DG	Diacylglycerol/Diglyceride
ATP	Adenosine Triphosphate

TCA	Tricarboxylic Acid Cycle
MG	Monoacylglycerol/Monoglyceride

CHAPTER ONE

Introduction

Background

From complex organisms such as mammals down to single-celled fungi, the cost of sustaining life is particularly high and requires a continuous cycle of uptake, synthesis, and turnover of energy. Lipids serve as an exceptionally rich source of energy as they can be shunted into a variety of pathways to maintain cellular homeostasis, from powering the generation of ATP via the TCA cycle, to providing precursors for membrane synthesis, to their sequestration for future utilization during times of starvation or nutrient deprivation. Disregulation of the import, *de novo* synthesis, or catabolism of lipids has been linked to a number of cardiovascular, hepatic, and obesity-related diseases (Gluchowski et al., 2017; Olzmann and Carvalho, 2019).

Through a heavily conserved process, eukaryotes (and even select prokaryotes) store excess lipids in the form of cytosolic organelles known as lipid droplets (LD) (Walther et al., 2017). Long thought to be inert globules, LDs are *bona fide* organelles, critical for the maintenance of lipid and energy homeostasis. Prior to packaging into LDs, these accumulated lipids are modified into a non-toxic form known as neutral lipids (NL), of which there are two predominant species: Triacylglycerol (TG), which is comprised of 3 free fatty acids (FFA) esterified to a glycerol backbone and Sterol Ester (SE) which contains a single FFA esterified to a free sterol molecule (Walther et al., 2017). LDs have been better characterized in recent years through a combination of *in vivo* and *in vitro* studies that have identifited novel functions

for these organelles, outside of fat storage. Droplets have been implicated in the protection against lipotoxic and oxidative stresses, sequestration of vitamins and signaling lipid precursors, and as a platform for temporary docking of non-metabolic proteins (Listenberger et al., 2003; Hinson and Cresswell, 2009; Koliwad et al., 2010; Li et al., 2012; Welte, 2015). Collectively, these organelles serve as a nexus for maintaining cellular homeostasis on a multitude of levels.

While the mechanisms of LD biogenesis have long been the subject of intense study, a relatively new question has emerged: What determines LD identity? LDs are not homogenous and are in fact quite diverse. Distinguished by morphology, location within the cell, and proteome, LDs can be separated into unique subsets, or "subpopulations" on the basis of these characteristics (Thiam and Beller, 2017). Moreover, LD subpopulations have been identified across multiple species and have been shown to serve specific functions on the cellular level (Zhang et al., 2016; Thiam and Beller, 2017; Eisenberg-Bord et al., 2018; Hariri et al., 2019; Ugrankar et al., 2019; Schott et al., 2019). One major gap in knowledge has been to determine how these LD subpopulations are assigned distinct functions. Due the high level of conservation and ease of genetic manipulation, *Saccharomyces cerevisiae* (budding yeast) has proven to be a potent tool in unraveling the functional diversity of LD subpopulations.

My research focuses on using yeast to address the following questions: 1) What factors dictate the unique functions of LD subsets?, and 2) How do specific proteins target to some LDs over others? To this end, I have begun to characterize one such LD subpopulation and the its protein marker, Bsc2. The succinct literature review below covers the current understanding of several facets of the LD life cycle, specifically biogenesis, mechanisms of protein targeting,

and degradatation by lipolysis. In the context of the Bsc2-positive LD subset, my work defines a molecular basis for the ability of LD proteins to specifically target LDs enriched in TG as opposed to SE. Additionally, my studies implicate Bsc2 in the negative regulation of TG lipolysis. Collectively, I propose that Bsc2 demarcates a LD subpopulation, where it protects against premature lipolysis of TG, and sequesters these LDs for long-term starvation. My work establishes key insights into how cells mark LDs for specific functional tasks, on the molecular level.

Neutral lipid synthesis and lipid droplet (LD) biogenesis

Lipotoxicity, or accumulation of free fatty acids within cellular membranes, triggers various stress pathways, such as the unfolded protein response (UPR) in the ER, and is detrimental to overall cell health. In response, excess lipids can be shunted into neutral lipids, which are ultimately packaged into LDs, thereby protecting the cell from a lipotoxic state. The neutral lipid core of LDs is surrounded by a phospholipid monolayer and their surface decorated with variety of proteins that regulate both the synthesis and turnover of these organelles. LDs participate in a number of inter-organelle contacts, but the most extensive contacts are maintained with the ER, the membrane compartment from which they are derived. NLs are synthesized at the ER via the activity of specific acyltransferase enzymes that esterify an activated FA to either a free sterol molecule (ergosterol in yeast, cholesterol in mammals) to form SE or to a Diacylglycerol (DAG) molecule to form TG. In yeast, the diacylglycerol acyltransferases Dga1 and Lro1 (DGAT1 and DGAT2 in mammals) convert DAG to TG, while SEs are formed by sterol ester acyltransferases, Are1 and Are2 (ACAT1 and ACAT2, in

mammals). When all four yeast acyltransferases are deleted, cells are viable, but LDs are completely absent and these cells are susceptible to a number of metabolic stresses, in particular to starvation conditions (Sandager et al., 2002; Sorger et al., 2004; Gaspar et al., 2011; Velázquez et al., 2016).

LD biogenesis is a heavily coordinated process, involving a number of energetic, lipid, and protein factors that collectively enable these organelles to emerge from the ER. First, NLs are synthesized in the upper leaflet of the ER bilayer and once the concentration reaches more than ~>3 mol% (biochemical and molecular dynamics simulations suggest ~5-10 mol%), a coalesced lipid lens forms via a dewetting process (Khandelia et al., 2010; Duelund et al., 2013). NL accumulation within ER membranes drives the formation of these oil lenses in order to decrease surface tension at the cytosolic-face of the ER membrane and to prevent exposure of these newly formed hydrophobic molecules to the aqueous environment (Thiam and Forêt, 2016). Phospholipid composition of the ER has been shown to be decisive in the ability of these NL lenses to extend out towards the cytosol, a process known as “budding”. Specific phospholipid species like lyso-phospholipids favor the budding of coalesced NL as has been demonstrated via modeling and in vitro work (Thiam and Forêt, 2016; Ben M’barek et al., 2017). In addition, key cytosolic and ER proteins enrich at these NL lenses and contribute to the budding and expansion of LDs.

Heavily conserved across multiple organisms, Seipin is an ER-resident protein and widely considered to be a master regulator of LD biogenesis and expansion (Magré et al., 2001; Szymanski et al., 2007; Fei et al., 2008). For yeast, flies, and mammals, LD biogenesis is severely delayed in seipin deletion mutants, and the LDs that do form display disturbed

morphology, characterized by a combination of small clustered LDs and fragile “super-sized” LDs (Fei et al., 2011; Cartwright et al., 2015; Wang et al., 2016). Biochemical work, paired with cryo-electron tomography (Cryo-ET) and computational modeling demonstrate that yeast, human, and fly Seipin assembles into an oligomeric ring at ER-LD contacts (Binns et al., 2010; Yan et al., 2018; Sui et al., 2018; Arlt et al., 2022). It is hypothesized that this self-assembly facilitates the flow of newly synthesized TG from the upper leaflet of the ER into nascent LDs, allowing these LD buds to expand and mature. Interestingly, yeast Seipin works in concert with an ER-localized binding partner, Ldb16, to promote successful LD biogenesis, and single deletion of Ldb16 mimics the LD morphology and phospholipid imbalance phenotypes of Seipin mutants (Wang et al., 2014; Grippa et al., 2015; Han et al., 2015; Wolinski et al., 2015; Klug et al., 2021; Renne et al., 2022).

In addition to Seipin, ER-localized fat storage-inducing transmembrane (FIT) proteins have implicated in LD biogenesis. Mammals express FIT1 and FIT2, while FIT proteins in yeast are orthologs of only FIT2, known as Scs3 and Yft2 (Kadereit et al., 2008). Cross-species studies indicate that the FIT proteins are necessary for proper LD budding, as FIT deficient cells in mammals, worms, and yeast exhibit NL lens accumulation within the ER (Kadereit et al., 2008; Choudhary et al., 2015). More recently, it has been demonstrated that FIT2 is in fact acyl-CoA diphosphatase enzyme that appears to serve as a negative regulator of acyl-CoA accumulation in the ER lumen (Becuwe et al., 2020). As such, it is hypothesized that FIT protein-dependent maintenance of phospholipid species at the ER is crucial to promote successful LD budding.

As mentioned above, cytosolic proteins can be recruited to TG lenses during the initial steps of LD formation. The mammalian perilipin family of LD coat proteins have been shown to not only participate in the regulation of TG lipolysis, but also contribute to LD biogenesis (Sztalryd and Brasaemle, 2017). This function has been best demonstrated in in budding yeast, where LD biogenesis is coordinated in part by Pln1, an ortholog of mammalian perilipins (Gao et al., 2017). Loss of Pln1 results in significantly reduced TG levels, delayed LD biogenesis and structurally fragile LDs. Functionally, Pln1 is recruited to nascent TG LDs where it is thought to coat and provide structure at the cytosolic-facing LD monolayer (Gao et al., 2017). Following biogenesis and adequate expansion, mature LDs remain affixed to the ER in yeast, whereas in mammals it is possible for a portion of these organelles to completely separate from the ER membrane (Jacquier et al., 2011; Valm et al., 2017).

LD protein targeting

The proteome of LDs is quite diverse and not restricted to proteins involved in lipid metabolism and catabolism. In fact, proteins associated with membrane trafficking and proteasomal-dependent protein degradation have been shown to enrich on LDs in both yeast and mammalian proteomics studies (Athenstaedt et al., 1999; Binns et al., 2006; Grillitsch et al., 2011; Bersuker et al., 2018). The yeast LD proteome consists of roughly 35-40 proteins, while mammalian LDs are enriched with anywhere from 100 to 150 proteins (Currie et al., 2014; Bersuker et al., 2018).

Molecular dynamics simulation paired with *in vivo* and *in vitro* fluorescence imaging of LD-targeting proteins have revealed that most primarily utilize some version a hydrophobic

domain that mediates contact with naturally occurring gaps in the LD monolayer, known as "packing defects" (Bacle et al., 2017; Prévost et al., 2018). Ongoing studies are teasing apart the specific mechanisms of protein targeting to LDs, but the current understanding has defined two distinct types of protein classes that can associate with LDs: Class I and Class II (Kory et al., 2016; Olzmann and Carvalho, 2019). Class I proteins are generally ER resident proteins that move to and from LDs in response to metabolic triggers, while Class II proteins are cytosolic proteins that are targeted to the LD monolayer (Kory et al., 2016). Traditionally, Class I proteins contain a hydrophobic segment, specifically a predicted hairpin, that allows them to transition from association with the upper leaflet of the ER bilayer to the LD monolayer upon stimulation of LD biogenesis. Prime examples include lipid synthetic enzymes GPAT4 and DGAT2, and ERAD-associated factor UBXD8 in mammals, and the yeast enzymes Dga1 and Erg6 (Zehmer et al., 2009; Olzmann et al., 2013; Wilfling et al., 2013; Jacquier et al., 2011; Olarte et al., 2020).

Class II proteins are much more diverse in identity, and involve cytoplasm to LD targeting that is generally mediated by an amphipathic helix (or other hydrophobic helix), posttranslational addition of a lipid moiety, or a protein-protein interaction with a separate LD protein (Kory et al., 2016). As mentioned above, in response to elevating surface tension, packing defects are generated in the phospholipid monolayer of LDs. This in turn, exposes portions of the NL core and facilitates alpha helical association of certain Class II proteins with LDs. The perilipin family of coat proteins employ alpha helical repeats of varying lengths that, once in contact with a packing defect, fold into amphipathic helices containing opposed facing

hydrophobic and charged residues, and are sufficient to target to LDs (Rowe et al., 2016; Čopič et al., 2018; Giménez-Andrés et al., 2018; Pataki et al., 2018).

LD turnover via lipolysis

One of the primary roles of LDs are to serve as energy reservoirs. In response to various metabolic stimuli, the LD core lipids can be broken down to their base components of FFA, glycerol, and free sterol, and subsequently used to provide energy during nutrient limiting conditions or supply lipids for membrane building. This process can occur through autophagy (lysosomal degradation), or more commonly through a process known as lipolysis, which involves the targeting and breakdown of NL via cytosolic enzymes known as lipases (Zechner et al., 2017). In mammalian adipocytes, TG lipolysis is a highly regulated cascade of hydrolysis reactions, instigated by adipose triglyceride lipase, or ATGL (Zimmermann et al., 2004). Under fasted conditions, ATGL hydrolyzes a FA moiety from TG and generates diacylglycerol (DG), then hormone-sensitive lipase (HSL) converts DG to monoacylglycerol (MG), which is then broken down to glycerol and FA by monoglyceride lipase (MGL) (Vaughan et al., 1964). Interestingly, there appears to be some enzymatic promiscuity as HSL can also hydrolyze the cleavage of FAs from TG, DG, MG and even SE. Mechanistically, mammalian TG lipolysis is tightly controlled, involving changes at the transcriptional level and posttranslational modifications (like phosphorylation), that augment the activity of the TG lipases (Zechner et al., 2017). As the major TG lipase, ATGL has an added layer of enzymatic regulation through the competitive binding of either a peptide co-activator (CGI-58) or a peptide inhibitor (G0S2) (Lass et al., 2006; Yang et al., 2010; Zhang et al., 2017).

Much like mammals, budding yeast rely on the same heavily conserved protein machinery to catabolize their LDs via lipolysis. During times of active cell growth, such as LOG phase, or acute nutrient deprivation, yeast use their three paralogous lipases Tgl3, Tgl4, and Tgl5 to hydrolyze TG and supply the cell with FA (Athenstaedt and Daum, 2003, 2005). Structurally, Tgl3, Tgl4 and Tgl5 all share features common to lipolytic enzymes such as ATGL, specifically a patatin domain as well as the conserved lipase motif, GXSXG. Furthermore, Tgl3 (and to a lesser extent, Tgl4) can catabolize DG to MG and there are no known DG-specific lipases in yeast (Kurat et al., 2006). Yju3, a separate enzyme and functional ortholog of mammalian MG lipase, catalyzes the final cleaveage of MG to FA and glycerol (Heier et al., 2010). Although all of the Tgl lipases can use TG as a substrate, previous work has demonstrated that Tgl3 is the predominant yeast TG lipase. Tgl3 not only displays the most TG lipolysis activity *in vitro* and *in vivo*, but Tgl3 mutant yeast contain drastically elevated whole-cell TG levels (Athenstaedt and Daum, 2005). Despite the shared homology with mammals, far less is known regarding the regulatory mechanisms of TG lipolysis in yeast. Previous biochemical studies have demonstrated that the LD-targeting and stability of Tgl3 is dependent on the presence of NLs, specifically TG (Schmidt et al., 2013). In the absence of TG, Tgl3 is re-targeted the ER where it loses lipolytic activity and is rapidly degraded.

Hypothesis

Over past two decades, significant strides have been made in understanding the multitude of physiological functions performed by LDs, including, but not limited to: providing energy during nutrient deprivation, protection against lipotoxicity, and even the

coordination of tissue development. *In vivo* studies have identified functionally distinct LD pools, or subpopulations, that are thought to be a cellular compensatory mechanism for the variety of aforementioned tasks. As previously discussed in the background of this section, major open questions in regards to LD diversity are: 1) What factors dictate the unique functions of LD subsets?, and 2) How do specific proteins target to some LDs over others?

My doctoral work, described in the pages below, focuses on delineating the interplay between the protein identity of select LD pools and their function, in the context of the yeast LD protein, Bsc2. **I hypothesize that Bsc2 targets a TG-enriched LD subpopulation, where it negatively regulates TG lipolysis, and in turn, conserves this LD pool for use during long-term starvation conditions.**

Using fluorescence microscopy, I have demonstrated that Bsc2 specifically localizes to a LD subset during active, or logarithmic growth, and these distinct group of LDs are TG-rich, as Bsc2 fails to adequately target SE-rich LDs. Combining live-cell imaging with state-of-the-art molecular dynamics (MD) simulations, we find that Bsc2 localizes specifically to TG-enriched LDs via two unique hydrophobic regions (HRs). Furthermore, these MD simulations reveal that Bsc2's HRs undergo distinct conformational changes on TG-enriched LDs compared to SE-enriched LDs, where key polar residues mediate and stabilize this Bsc2-TG interaction. Through biochemistry and yeast genetics, I also show that Bsc2 is a novel regulator of TG lipolysis, where it inhibits the main TG lipase, Tgl3. Bsc2 deletion yeast display elevated lipolysis and an LD defeceit during long-term starvation, whereas overexpression of Bsc2 results in a drastic accumulation of whole-cell TG and giant LDs. As such, by deorphanizing Bsc2 and its targeted LD subset, I challenge current understanding of

lipolysis in yeast by proposing that LDs are not mobilized equally in response to metabolic cues, but are differentially sequestered. Collectively, my thesis work provides a novel role for LD subpopulations in the maintenance of cellular homeostasis.

CHAPTER TWO

Bsc2 is a novel regulator of triglyceride lipolysis that demarcates a lipid droplet subpopulation

Abstract

Cells store lipids in the form of triglyceride (TG) and sterol-ester (SE) in lipid droplets (LDs). Distinct pools of LDs exist, but a pervasive question is how proteins localize to and convey functions to LD subsets. Here, we show the yeast protein Bsc2 localizes to a subset of TG-containing LDs, and reveal it negatively regulates TG lipolysis. Mechanistically, Bsc2 LD targeting requires TG, and LD targeting is mediated by hydrophobic regions (HRs). Molecular dynamics simulations reveal these Bsc2 HRs interact with TG on modeled LDs, and adopt specific conformations on TG-rich LDs versus SE-rich LDs or an ER bilayer. Bsc2-deficient yeast display no defect in LD biogenesis, but exhibit elevated TG lipolysis dependent on lipase Tgl3. Remarkably, Bsc2 abundance influences TG, and over-expression of Bsc2, but not LD protein Pln1, promotes TG accumulation without altering SE. Finally, we find Bsc2-deficient cells display altered LD mobilization during stationary growth. We propose Bsc2 regulates lipolysis and localizes to subsets of TG-enriched LDs.

Introduction

Lipid droplets (LDs) are fat storage organelles comprised of a neutral lipid core containing both triglycerides (TG) and sterol esters (SE) (Walther et al., 2017). Distinct from

bilayer-bound organelles, LDs are surrounded by a phospholipid (PL) monolayer which is decorated with surface proteins that aid in their biogenesis and degradation (Currie et al., 2014). These cytosolic lipid reservoirs can be made or broken down in response to a variety of metabolic cues, such as nutrient deprivation or increased membrane biogenesis. Defects in lipid storage in LDs contribute to numerous metabolic disorders including obesity, cardiovascular disease, and diabetes (Welte, 2015; Gluchowski et al., 2017). Recent studies indicate that beyond their role in lipid storage, LDs also play important roles in signaling and protein homeostasis (Li et al., 2012; Bersuker et al., 2018; Schmeisser et al., 2019). Despite this, it remains unclear if distinct pools of LDs exist within cells to enable this functional diversity. Work from our group and others have shown that LDs are not homogenous within the context of a single cell, but exist in a variety of subpopulations that contain distinct proteomes and/or morphologies (Zhang et al., 2016; Eisenberg-Bord et al., 2018; Teixeira et al., 2018; Schott et al., 2019; Ugrankar et al., 2019). Although LDs exhibit these unique features, little is currently known regarding how such differences dictate LD function. LD subpopulations are of particular interest to the field of metabolism as there is mounting evidence that different LD pools play roles in maintaining metabolic homeostasis in response to various nutrient states (Hariri et al., 2018; Eisenberg-Bord et al., 2018; Teixeira et al., 2018). For example, large and small LD pools observed in human hepatocytes are mobilized by mechanistically distinct pathways during starvation (Schott et al., 2019). Similarly, *Drosophila* fat body cells contain two subpopulations of LDs that are differentially maintained by extracellular and *de novo* synthesis of lipids (Ugrankar et al., 2019).

LD turnover primarily occurs through a highly conserved process known as lipolysis. This catabolic process involves the targeting of cytoplasmic lipases to LDs where they hydrolyze TG and SE to base components. TG breakdown via lipolysis is necessary for maintaining lipid homeostasis, sustaining membrane biosynthesis, and promoting cellular division across multiple species (Duncan et al., 2007; Schmidt et al., 2014; Heier and Kühnlein, 2018). However, the underlying mechanisms for regulation of TG lipolysis in budding yeast are poorly understood. Yeast contain three LD-resident and paralogous TG lipases: Tgl3, Tgl4, and Tgl5 (Athenstaedt et al., 1999; Athenstaedt and Daum, 2003, 2005; Kurat et al., 2006). Although Tgl4 has been shown to be the functional ortholog of the mammalian TG lipase, ATGL, in yeast, it is in fact Tgl3 that performs the bulk of the lipolytic activity *in vivo* as it can hydrolyze TG species of variable fatty acid chain length (Athenstaedt and Daum, 2003, 2005; Kurat et al., 2006). The regulation of Tgl3-mediated TG lipolysis is poorly understood. Previous studies provide some insight by demonstrating that in the absence of either TG or LDs as whole, Tgl3 activity, targeting, and stability is negatively impacted, a common trait for many resident LD proteins (Schmidt et al., 2013; Koch et al., 2014). In LD-null yeast, Tgl3 is re-targeted to the ER where it loses its lipolytic activity and is rapidly degraded (Schmidt et al., 2013). In spite of this information, specific regulators of Tgl3 TG lipase activity remain unidentified. Whether specific LD subsets are preferentially mobilized during metabolic cues is also underexplored.

Here, we deorphanize and characterize the LD protein Bsc2 as a negative regulator of TG lipolysis in yeast. We show that Bsc2 enriches on a subpopulation of LDs at logarithmic (LOG) phase yeast growth. We find Bsc2 LD targeting is dependent on the presence of TG, as

Bsc2 fails to stably localize to SE-LDs. Structure-function analysis reveals the N-terminal half of Bsc2, containing distinct hydrophobic domains, is necessary for stable LD association. This is supported by molecular dynamics (MD) simulations that demonstrate Bsc2 adopts a distinct conformational ensemble on TG-rich LDs and interacts extensively with TG in addition to LD monolayer PLs. Physiologically, loss of Bsc2 (*bsc2*Δ) generates a significant decrease in steady-state TG during yeast LOG phase growth. We show this decrease is not due to reduced TG synthesis, but rather from upregulated Tgl3-dependent TG lipolysis. Notably, Bsc2 over-expression promotes TG accumulation and LD enlargement in yeast, but does not alter SE pools. We propose that Bsc2 demarcates a LD subpopulation, where it locally inhibits Tgl3-dependent TG lipolysis.

Results

Bsc2 localizes to a LD subset and requires TG for LD targeting

To dissect how proteins target to specific lipid droplets (LD) subpopulations, we used a candidate-based approach to image GFP-tagged proteins annotated to localize to LDs in the budding yeast *Saccharomyces cerevisiae*. We manually imaged yeast expressing these chromosomally GFP-tagged proteins and co-expressing the canonical LD protein Erg6-mRuby, a previously established LD marker known to decorate all yeast LDs (Müllner et al., 2004). Candidate-based imaging revealed that Bsc2-GFP, a canonical LD targeting protein of unknown function, was detected on only a subset of Erg6-mRuby labeled LDs in yeast growing at logarithmic (LOG) phase (**Figure 2.1A**). Similarly, LOG-phase yeast expressing Bsc2-GFP

and stained with the general LD dye monodansylpentane (MDH) also showed partial MDH and Bsc2-GFP co-localization (**Figure 2.1C**). Consistent with this, previous work also determined that Bsc2 was among a few LD proteins detected on only LD subsets in budding yeast (Eisenberg-Bord et al., 2018; Teixeira et al., 2018). To determine whether Bsc2-GFP decorated a LD subset in yeast in different growth phases, we also imaged yeast grown into stationary (STAT) phase, when cell growth slows and LD lipid storage is elevated. STAT phase yeast also exhibited detectable Bsc2-GFP on LDs, but this Bsc2-GFP signal colocalized closely with Erg6-mRuby (**Figure 2.1A**). Quantification of this Bsc2-GFP/Erg6-mRuby colocalization in LOG and STAT phases revealed that in LOG phase, only ~40% of Erg6-mRuby LDs also exhibited detectable Bsc2-GFP (**Figure 2.1B**). In STAT phase this detectable co-localization increased to ~70%, suggesting Bsc2-GFP and Erg6-mRuby colocalization increased in STAT phase.

Recent work indicates that LD neutral lipid composition can influence protein targeting to the LD surface (Thiam and Beller, 2017; Chorlay and Thiam, 2020; Caillon et al., 2020; Dhiman et al., 2020). Since yeast LDs contain TG and SE, we next dissected whether loss of either of these neutral lipids influenced Bsc2-mNeonGreen (Bsc2-mNG) LD localization. We generated a chromosomally-tagged Bsc2-mNG yeast strain that produced only TG (TG-only) by deleting the genes encoding the two SE-generating enzymes Are1 and Are2, and a strain producing only SEs (SE-only) by deleting the TG-synthesis enzymes Dga1 and Lro1 (Sandager et al., 2002; Sorger et al., 2004). Imaging revealed that whereas the wildtype (WT) and TG-only yeast exhibited Bsc2-mNG that co-localized with a subset of LDs, the SE-only yeast contained very dim Bsc2-mNG signal that was nearly undetectable on LDs (**Figure 2.1D**).

This suggests that TG is necessary for Bsc2-mNG LD targeting, and potentially for Bsc2-mNG protein stability.

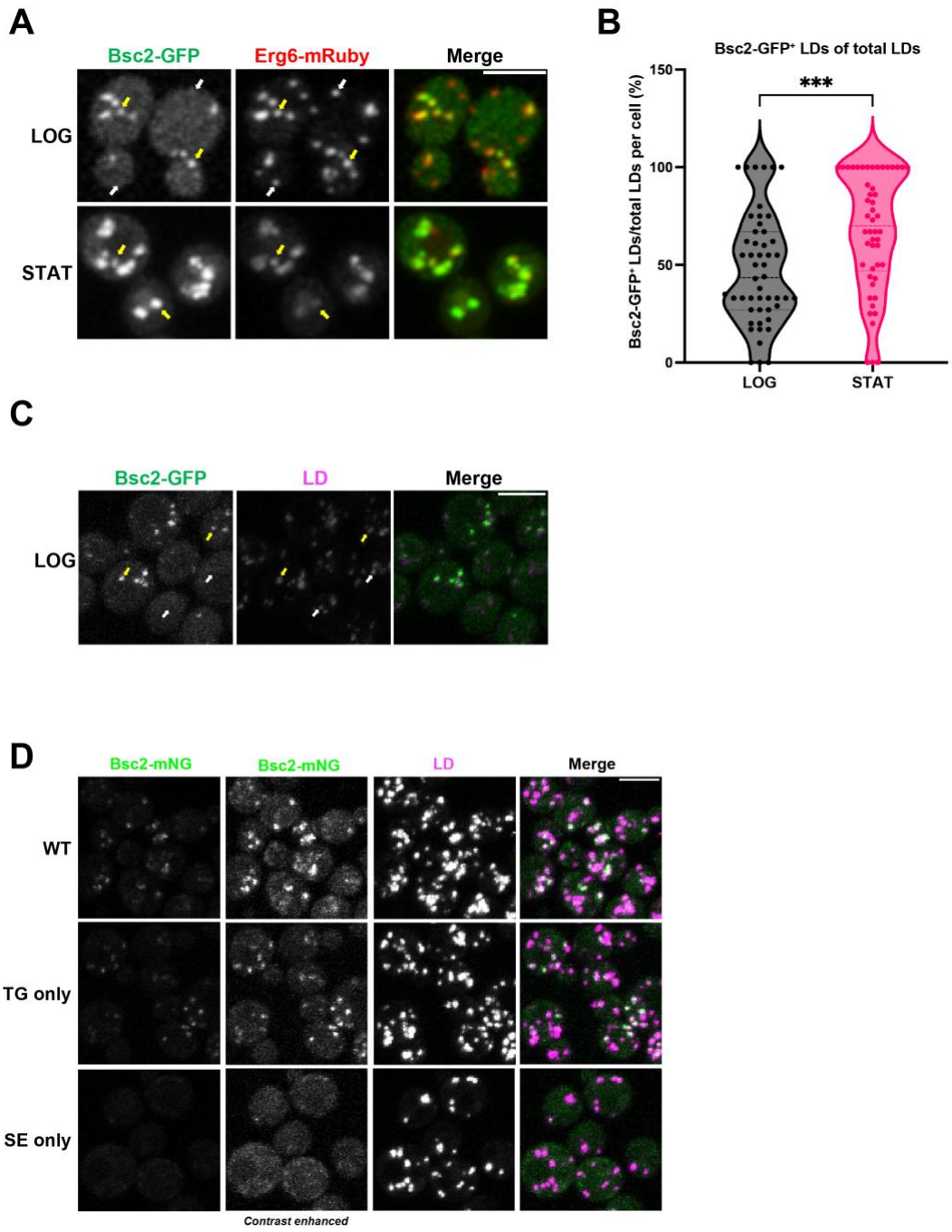

Figure 2.1. Bsc2 enriches on a TG-containing LD subpopulation at logarithmic phase.
(A) Logarithmic (LOG) and stationary (STAT) phase imaging of yeast dual-tagged for Bsc2-GFP, Erg6-mRuby. Yellow arrows indicate Bsc2-enriched LDs and white arrows indicate LDs where Bsc2 is undetectable or absent.
(B) Quantification of percentage of Bsc2-positive ($Bsc2^{+}$) LDs out of total Erg6-mRuby LDs, per cell, at LOG and STAT phase. For both LOG and STAT samples, n = 50 cells.
(C) Bsc2-GFP expressing yeast stained with LD dye MDH and imaged at LOG phase growth. Yellow arrows are Bsc2-positive LDs, white arrows denote Bsc2-negative LDs.
(D) Imaging of Bsc2-mNeonGreen (Bsc2-mNG) yeast in different neutral lipid-containing backgrounds with MDH-stained LDs at LOG phase. TG = Triglyceride, SE = Sterol Ester. Far left column represents non-contrast adjusted images for Bsc2-mNG. Statistics represent Unpaired t test with Welch's correction. ***, $P < 0.001$. Scale bars, 5μm.

The Bsc2 N-terminal hydrophobic regions mediate LD targeting

Proteins can target to LDs through amphipathic or hydrophobic motifs that interact with or insert into the LD PL monolayer (Bacle et al., 2017; Prévost et al., 2018; Chorlay and Thiam, 2020; Chorlay et al., 2021). To mechanistically dissect how Bsc2 targets to LDs, we examined its hydrophobicity using Phobius (Käll et al., 2004) (**Figure 2.2A**). The hydrophobicity plot predicted two hydrophobic regions in the N-terminal half of Bsc2, which we denote as Hydrophobic Region 1 (HR1) and Hydrophobic Region (HR2). Bsc2 also contains a predicted Low Complexity Region (LCR) directly downstream of these HRs. We hypothesized that Bsc2 targets to LDs through the action of either HR1, HR2, or both regions. To test this, we generated seven mNG-tagged fragments of Bsc2, and over-expressed them in yeast stained for LDs in LOG phase growth (**Figure 2.2B**). Interestingly, full length Bsc2 ($Bsc2^{FL}$) targeted both LDs and the endoplasmic reticulum (ER) when over-expressed. Similarly, a truncated fragment removing the LCR ($Bsc2^{N\text{-}HR1+HR2}$) also showed this LD and ER dual-targeting, as did a smaller fragment only containing the HR1 and HR2 regions ($Bsc2^{HR1+HR2}$), suggesting

the LCR and N-terminal region ($Bsc2^{N}$) preceding HR1 are not necessary for this LD/ER localization.

Next we dissected how HR1 and HR2 influence Bsc2 localization to the ER network and LDs. A construct encoding only the N-terminal region and HR1 ($Bsc2^{N\text{-}HR1}$) localized to LDs, suggesting HR1 may be sufficient for LD targeting (**Figure 2.2B**). In support of this, amino acid and secondary structure analysis of HR1 indicates it forms a predicted alpha-helical fold, with several hydrophobic amino acids on one face, commonly observed in LD targeting motifs (**Figure 2.2A**). A smaller construct retaining HR1 without the preceding N-terminal region ($Bsc2^{HR1}$) failed to express well in yeast, suggesting the initial N-terminal region may be necessary for HR1 stability. Surprisingly, a construct encoding only HR2 ($Bsc2^{HR2}$) localized primarily to the ER network surrounding the nucleus and peripheral ER (**Figure 2.2B**). No detectable LD localization was detected for $Bsc2^{HR2}$, indicating HR1 was necessary for detectable LD targeting. Since HR1 appeared to mediate the Bsc2 LD interaction, we generated a chimeric Bsc2 construct where we replaced HR1 with LiveDrop ($Bsc2^{LiveDrop}$), a known LD targeting module derived from the LD targeting motif of *Drosophila* GPAT4 (Wilfling et al., 2013; Wang et al., 2016). Indeed, $Bsc2^{LiveDrop}$ targeted to LDs as well as the ER network when over-expressed in yeast, and appeared similar to $Bsc2^{FL}$, suggesting LiveDrop could replace HR1 for organelle targeting (**Figure 2.2B**).

Bsc2 LD targeting could, in principle be due to direct insertion or interaction with the LD surface monolayer, or through binding another LD surface protein. To delineate these possibilities, we expressed yeast Bsc2-GFP in human U2-OS cells treated with oleic acid (OA) to induce LD biogenesis. Bsc2-GFP decorated the surfaces of LDs in U2-OS cells, suggesting

it was able to localize to the LD surface independent of other yeast proteins (**Figure 2.2C**). Collectively, this supports a model where Bsc2 interacts directly with the LD surface.

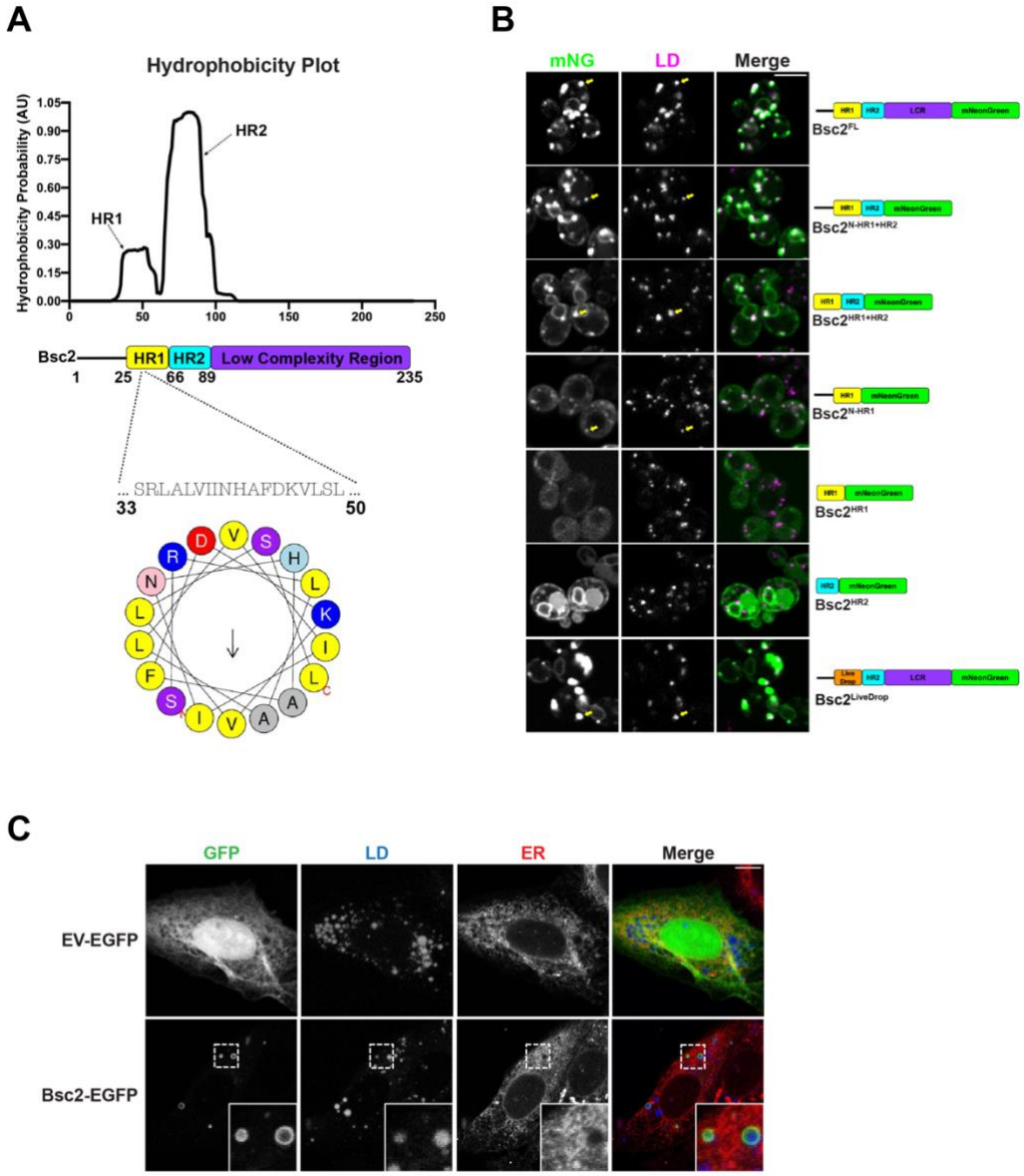

Figure 2.2. Hydrophobic Region 1 (HR1) of Bsc2 is responsible for LD-targeting.
(A) Hydrophobicity plot generated by Phobius online transmembrane topology and signal peptide predictor (top), paired with a schematic of Bsc2 protein architecture (middle), and a helical wheel of the Bsc2 amphipathic segment in HR1 (bottom). HR1 = Hydrophobic Region 1, HR2 = Hydrophobic Region 2.
(B) Log phase imaging of yeast over-expressing various Bsc2-mNG truncations with LDs stained with MDH. Yellow arrows indicate LD-targeting. LCR = Low Complexity Region.
(C) Imaging of U2-OS cells transiently overexpressing either empty vector (EV-EGFP) or Bsc2, both tagged with EGFP (Bsc2-EGFP) and treated with oleic acid (OA), overnight to induce LD formation. Cells were coIF stained with α-EGFP (green), α-HSP90B1 (ER, red), and LDs stained with MDH (blue) and imaged with confocal microscope. Inset shows Bsc2-LD targeting. Mammalian scale bar, 10 µm. Yeast scale bar, 5µm.

Molecular dynamics simulations suggest Bsc2 HRs adopt specific conformations on TG-rich LDs

To better understand the interaction between Bsc2 and LDs, molecular dynamics (MD) simulations were conducted with $Bsc2^{N\text{-}HR1+HR2}$ (residues 1-100) interacting with a TG-rich LD (TG-only), a SE-rich LD (90:10 ratio of cholesteryl oleate (CHYO) to TG), and an ER bilayer. The structure of $Bsc2^{N\text{-}HR1+HR2}$ was first predicted with RoseTTAFold (Baek et al., 2021) and AlphaFold2 (Jumper et al., 2021), both of which predicted an alpha-helix for HR1, and a hairpin (helix-kink-helix) conformation for HR2. TOPCONS (Tsirigos et al., 2015) and TM AlphaFold (Dobson et al., 2023) also predicted a membrane-embedded topology for the hydrophobic HR2 sequence (**Supplementary Figure 2.3M**). Although they were very similar, the RoseTTAFold structure was selected for further simulations as it has been demonstrated to better predict membrane structures (Azzaz et al., 2022; Hegedűs et al., 2022).

The membrane embedded systems were set up with the HR2 hairpin inserted into each respective lipidic environment deep enough to enable the charged residues on the ends (Arg61, Asp90, Asp93, Arg100) to be surface oriented where they can interact with the charged lipid headgroups and water (**Figure 2.3A, Supplementary Figure 2.3C**). The HR1 region was positioned 5 angstroms above the membrane PL to allow for membrane association between the amphipathic region and membrane packing defects (see Methods). Long timescale simulations were run on Anton2 provided by Pittsburg Supercomputing Center (Shaw et al., 2014), yielding 4.5 microseconds of simulations for the TG-only LD and ER bilayer systems. The 90:10 CHYO:TG LD system was run for 1 microsecond on EXPANSE provided by San Diego Supercomputing Center (Strande et al., 2021).

Simulations revealed clear conformational changes in Bsc2 between the LD and bilayer environments (**Figure 2.3A, Supplementary Figure 2.3A-C**). In both the TG-only and 90:10 CHYO:TG LDs, HR2 orients with the predicted helix-kink-helix angle of approximately 100°, then decreases to an angle of 70°, as the kink region engages with the TG core (**Supplementary Figure 2.3A-C**). In contrast, in the ER bilayer the helix-kink-helix region opens to an average angle of 150°, bringing the residues in the kink region closer to the PL surface (**Figure 2.3A**). A central driving force for this conformational change is the stabilization of polar residues Gln72, Cys75 and Ser76 near the kink of HR2. In the LDs, these residues interact with TG glycerol groups 2.0-2.5nm below the headgroup phosphates (**Figure 2.3B,C, Suplementary Figure 2.3D**). In the ER bilayer, stabilization at this depth is not possible as it places the polar residues in the hydrophobic tail region of the PLs (**Supplementary Figure 2.3E, F**). By splaying open, the kink region rises closer to the lipid head-groups, enabling polar interactions with the PL-glycerols ~1-1.2nm below the phosphate plane. Thus, HR2 obtains a kinked conformation in the LD monolayers, but a splayed open conformation in the ER bilayer.

The Bsc2 HR1 amphipathic helix embeds well in the packing defects of both the TG-rich LD and the ER bilayer (**Figure 2.3A**). The hydrophobic residues along the bottom of HR1 interact with both PL and TG acyl tails, while the charged and polar residues along the top stabilize the HR1 helix via hydrogen bonds with the PL headgroups and water. Strikingly, this is not the case for the 90:10 CHYO:TG LD. Here the HR1 helix fails to associate with the monolayer, and instead folds over on itself to maintain some degree of amphipathic interactions (**Figure 2.3A, right**). The reason for this discrepancy is insufficient lipid packing

defects in the SE-rich LD to adequately absorb the HR1 hydrophobic moieties (**Figure 2.3A, Supplementary Figure 2.3H-J**). Importantly, the amphipathic helix HR1 associates well with the TG-rich LD and ER bilayer, but fails to associate at all with the SE-rich LD.

Based on these simulations, the driving force for Bsc2 LD targeting is likely a combination of the Bsc2 HR1 and HR2 sequences working together. Due to its drastically different confirmation on TG-rich versus SE-rich (90:10 CHYO:TG) LDs, it is possible that HR1 may act as a 'sensor', detecting the numerous packing defects found on TG-rich LDs preferentially over SE-rich LDs and the ER bilayer. HR1 itself also interacts with the glycerol backbones of several TG molecules in the TG-rich LD system. Indeed, TG-rich LDs have been shown to have larger and longer-lived packing defects than the ER bilayer, with TG-LDs and ER-bilayers maintaining a packing defect constant of 27$\underline{|Å^2}$ and 16$\underline{|Å^2}$, respectively (Kim et al., 2021; Braun and Swanson, 2022). This discrepancy is even more pronounced for the SE-rich LD, which has a more densely packed PL monolayer with very few packing defects, maintaining a defect constant of 14$\underline{|Å^2}$ (Braun and Swanson, 2022). Collectively, the preferential targeting of HR1 to TG-enhanced packing defects would potentially explain why the over-expressed $Bsc2^{N\text{-}HR1}$ fragment localizes to LDs, and also provides a potential molecular explanation for why Bsc2 localizes to TG-rich LDs, but appears significantly less detectable on SE-rich LDs *in vivo*.

The hydrophobic HR2 segment seems to embed in either the ER bilayer or LD monolayers. We hypothesize that in the absence of HR1, HR2 likely remains in the ER, kinetically trapped in an interfacial conformation, as observed when $Bsc2^{HR2}$ is over-expressed in yeast. However, in the presence of HR1, HR2 may fold into a more stable kinked

conformation once the polar residues (Gln72, Cys75, Ser76) gain access to the glycerol groups of TG molecules in the LD core (**Figure 2.3A**). This is supported by the depth profile of Gln72, Cys75 and Ser76 in the TG-rich LD (**Supplementary Figure 2.3E**). Additionally, radial distribution functions (RDF) and coordination numbers $\overline{\| s \|}$ verify there are strong interactions between Gln72 and Ser76 especially to TG oxygens, while the hydrophobic residues surrounding these polar residues are still stabilized by PL tails (**Figure 2.3B-D**). In contrast, in the ER bilayer the HR2 region opens into a more shallow interfacial conformation below the PL headgroups because of the high barrier for the polar residues to enter the PL tail region (**Supplementary Figure 2.3F**). The relative stability of these two regions is captured in the potential of mean force (PMF) profiles (**Supplementary Figure 2.3G**), demonstrating that Gln72 and Ser76 are most stable slightly below the PL phosphate groups, where the polar backbone and sidechain can create favorable interactions with the polar PL components. Indeed, pulling them into the lipid tail region is highly unfavorable. Considering Ser76 alone, moving from its interfacial position (~1.0 nm below the phosphate plane) to a LD kinked position (~2 nm below) would cost ~30 kJ/mol. Such high penetration barriers may explain why $Bsc2^{HR2}$ remains localized in the ER bilayer. Thus, the dynamic interplay between residues keeps the HR2 region stable within the ER bilayer, kinetically trapped in the absence of HR1, but also offers a stabilizing force in the presence of HR1, which could overcome those barriers to enable HR2 to transition to a more stable LD conformation with both polar and hydrophobic residues adopting more optimal interactions.

It is also notable that Bsc2 interacts with many TG molecules in the TG-rich LD system. HR2 coordinates with the TG-glycerol backbone, and HR1 forms several contacts with TG

hydrophobic tails that intercalate into the PL monolayer (**Figure 2.3C,D, Supplementary Figure 2.3H-L**). Thus, the LD core appears to require an abundance of TGs for optimal Bsc2 interactions. The proportion of conformations with a TG molecule directly interacting with a residue captures the abundance of these interactions (**Supplementary Figure 2.3L**). The dominance of TG-interactions in the HR2 region demonstrates the sequence disposition to immerse itself within a TG-rich LD core. Additionally, the number of contacts between HR1 and TG-tails is a significant addition to its interactions with the PL-tails (**Supplementary Figure 2.3J**). Collectively, these simulations indicate that Bsc2 adopts significantly different conformational ensembles in the ER bilayer and LD environments, and that it interacts with TG molecules extensively in TG-rich LDs (**Figure 2.3E**). This provides a potential molecular explanation for Bsc2 preferentially targeting to TG-rich LDs.

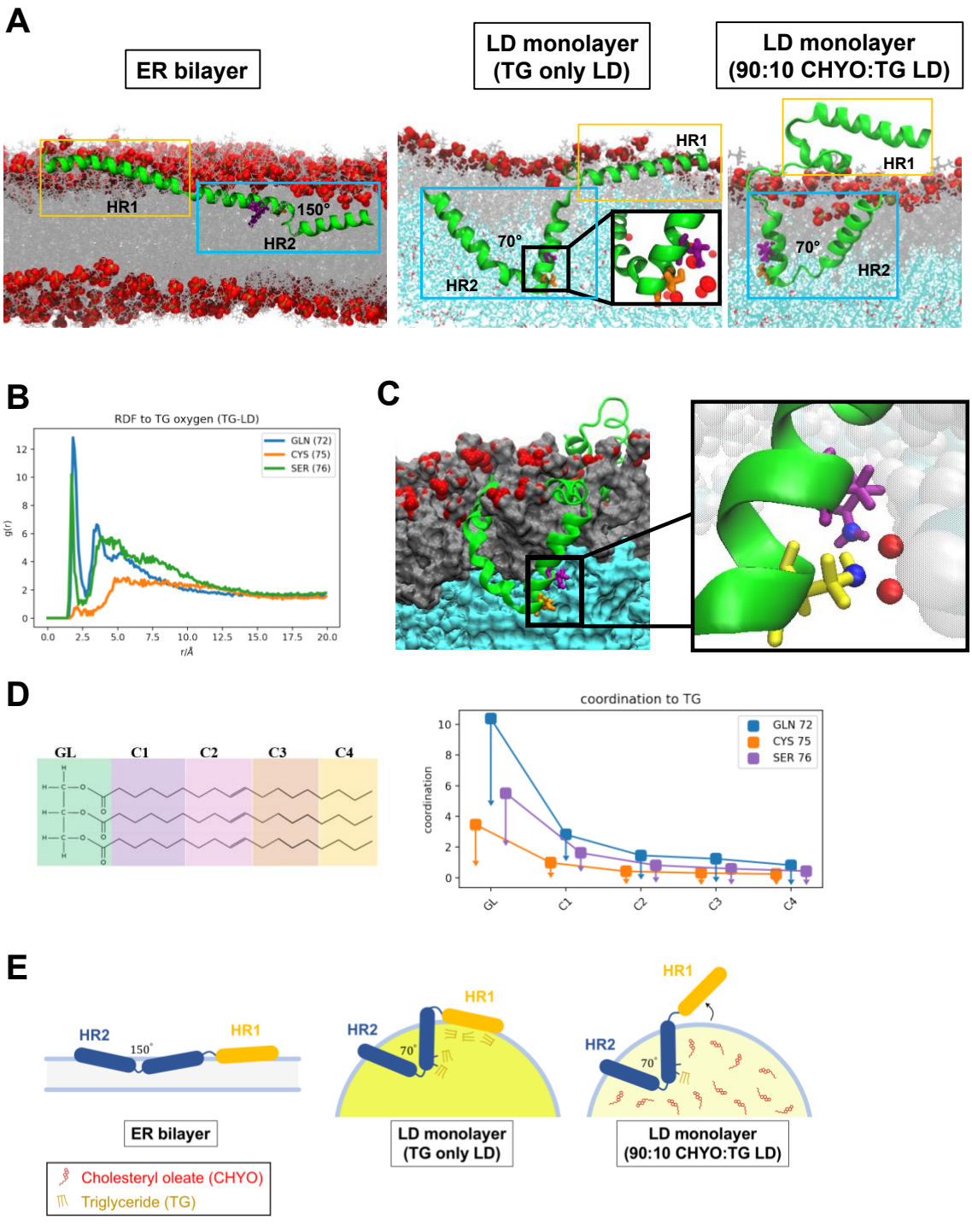
A
ER bilayer
LD monolayer (TG only LD)
LD monolayer (90:10 CHYO:TG LD)
HR1
HR2
150°
70°
B
RDF to TG oxygen (TG-LD)
GLN (72)
CYS (75)
SER (76)
g(r)
r/Å
C
D
GL
C1
C2
C3
C4
coordination to TG
GLN 72
CYS 75
SER 76
coordination
E
ER bilayer
LD monolayer (TG only LD)
LD monolayer (90:10 CHYO:TG LD)
Cholesteryl oleate (CHYO)
Triglyceride (TG)

Figure 2.3. Molecular dynamics simulations indicate Bsc2 adopts a unique conformational ensemble on TG-rich LDs

(A) In the modeled ER bilayer (left), the HR2 sequence opens to allow polar residues in the kink to evade the unfavorable phospholipid (PL) tail region. In the TG-rich LD (middle) polar residues (purple and orange) are stabilized by TG glycerol groups in the LD core. In the SE-rich LD (right), HR2 retains a kinked conformation with polar residues stabilized by Cholesteryl oleate (CHYO) oxygens in the LD core. Notably, the amphipathic HR1 sequence fails to LD associate due to significantly decreased packing defects.

(B) Radial distribution functions (RDF) of GLN, CYS, and SER in the HR2 interacting with TG glycerol oxygens.

(C) Cross section of the LD monolayer highlights interactions between GLN72 (purple), SER76 (yellow) and TG oxygens (inset).

(D) The coordination number between residue heavy atoms and different sections of the TG molecules verifies that most interactions are with the glycerol (GL) group. (E) Schematic of modeled $Bsc2^{N\text{-}HR1\text{-}HR2}$ adopting conformations in the ER bilayer, TG-rich LD, and SE-rich LD as in Panel A.

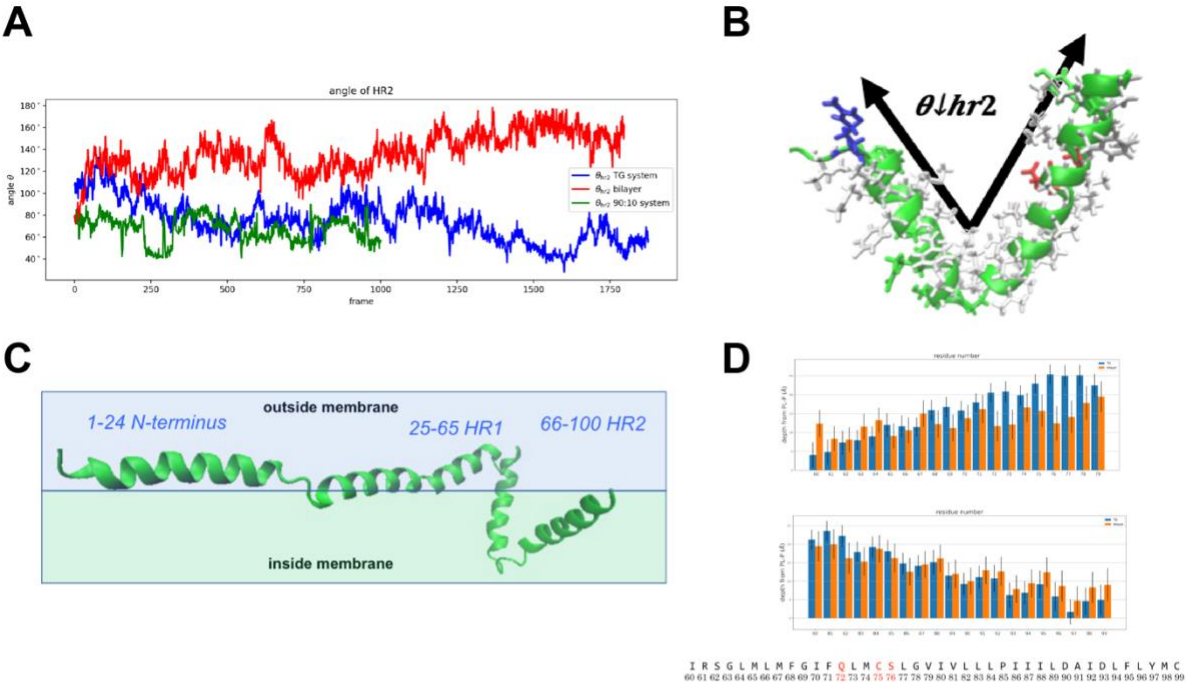
A
angle of HR2
angle θ
frame
θhr2 TG system
θhr2 bilayer
θhr2 90:10 system
B
θ↓hr2
C
outside membrane
1-24 N-terminus
25-65 HR1
66-100 HR2
inside membrane
D
residue number
I R S G L M L M F G I F Q L M C S L G V I V L L L P I I I L D A I D L F L Y M C
60 61 62 63 64 65 66 67 68 69 70 71 72 73 74 75 76 77 78 79 80 81 82 83 84 85 86 87 88 89 90 91 92 93 94 95 96 97 98 99

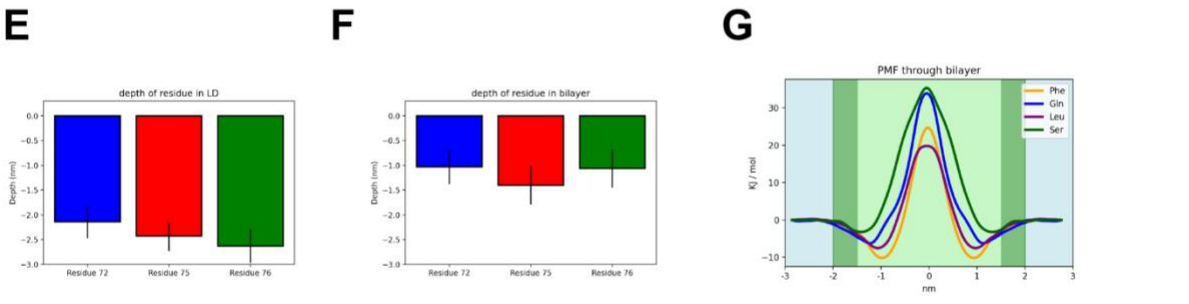
E
depth of residue in LD
Depth (nm)
Residue 72
Residue 75
Residue 76
F
depth of residue in bilayer
G
PMF through bilayer
Phe
Gln
Leu
Ser
kJ / mol
nm

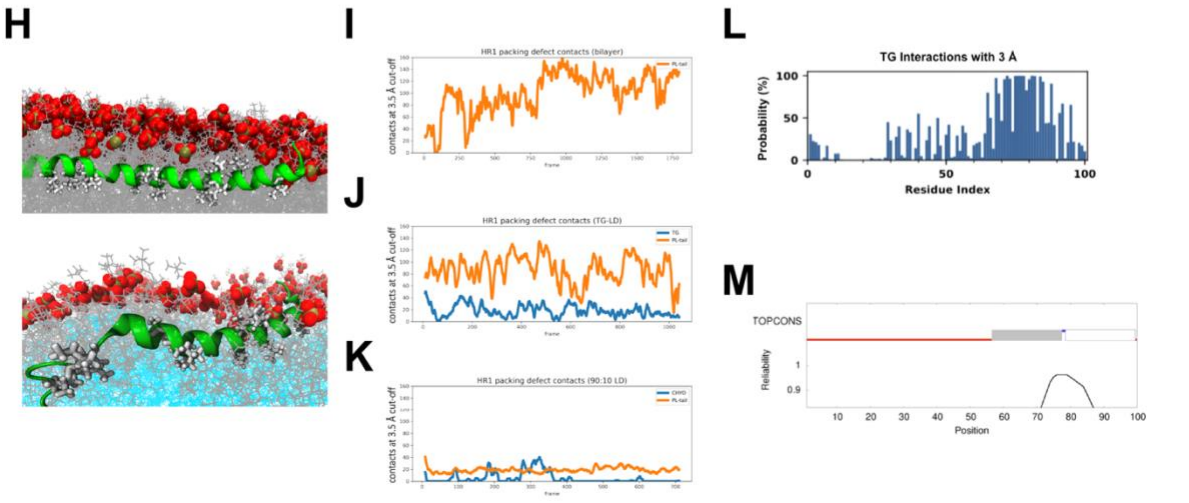
H
I
HR1 packing defect contacts (bilayer)
contacts at 3.5 Å cut-off
frame
J
HR1 packing defect contacts (TG-LD)
K
HR1 packing defect contacts (90:10 LD)
L
TG Interactions with 3 Å
Probability (%)
Residue Index
M
TOPCONS
Reliability
Position

Supplementary Figure 2.3. MD analysis of Bsc2 HR1 and HR2 conformations.
(A) The angle of HR2 over time in simulation.
(B) Schematic of HR2 helix-kink-helix region. The coordinates of the angle were taken between the endpoints (residues 61 and 100) and the kink (residue 78). The predicted/initial angle was 100 degrees.
(C) The predicted structure of Bsc2 N+HR1+HR2 through RoseTTAFold.
(D) Average depths from of residues 60-99 (sidechains) below the PL phosphate plane in the TG-rich LD and ER bilayer.
(E) Average depth of HR2 polar residues in the TG-LD
(F) Average depth of HR2 polar residues ER bilayer.
(G) The free energy profile for membrane permeation shows the stability of GLN and SER ~1nm below the phosphate plane just under the headgroups (dark green regions) and unfavorable penalty for pulling them ~2 nm below the plane into the PL tail region (light green region).
(H) HR1 sequence interacting with the bilayer (top) and TG-LD (bottom).
(I) In the ER bilayer, these contacts are all PL-tail interactions.
(J) In the TG-LD system, there is a combination of PL-tail and TG defects interactions.
(K) In the SE-rich 90:10 CHYO:TG LD, the interactions rarely occur as there are too few packing defects.
(L) The probability of each residue interacting with a TG molecule through the entire simulation. The HR2 sequence is almost in constant contact with TG molecules.
(M) TOPCONS prediction of transmembrane segments (grey and white bars), which correspond to the HR2 helices.

Loss of Bsc2 alters TG levels via enhanced TG lipolysis

Because Bsc2 LD targeting appeared to require TG, and MD simulations indicated Bsc2:TG interactions, we next determined whether manipulating Bsc2 expression influenced cellular TG pools. We first examined steady-state TG and SE levels of WT and *bsc2*Δ yeast. At LOG phase, *bsc2*Δ yeast display a ~20% steady-state reduction in TG compared to WT, while SE levels are unaffected (**Figure 2.4A**). We reasoned this TG reduction could be the result of either enhanced lipolysis or decreased TG synthesis (or a combination of both). To dissect this, we first tested whether TG lipolysis or TG biosynthesis was altered in *bsc2*Δ yeast. Yeast contain three TG lipases: Tgl3, Tgl4, and Tgl5, of which Tgl3 performs the majority of the TG lipolysis activity in the cell (Athenstaedt and Daum, 2003, 2005). To test whether TG lipolysis was altered in *bsc2*Δ yeast, we treated WT, *bsc2*Δ, *tgl3*Δ, and *bsc2*Δ*tgl3*Δ yeast with

cerulenin, which blocks *de novo* fatty acid synthesis and promotes TG lipolysis as a fatty acid source (**Figure 2.4B**). We then measured yeast TG levels before (T_0) and after 3hrs (T_3) of cerulenin treatment when lipolysis was active. Importantly, WT and *bsc2*Δ yeast contained similar TG levels at T_0, as we allowed yeast to grow for 24hrs into STAT phase and accumulate TG (**Figure 2.4C**). Notably, after 3hrs of cerulenin, WT yeast had ~60% of their TG stores remaining, whereas *bsc2*Δ only had ~20%, suggesting TG lipolysis was elevated in *bsc2*Δ yeast (**Figure 2.4C**). As expected, *tgl3*Δ yeast retained ~80% of their TG stores following 3hrs cerulenin (**Figure 2.4C**). In contrast to *bsc2*Δ yeast, *bsc2*Δ*tgl3*Δ yeast retained ~70% of their TG, behaving similar to *tgl3*Δ, suggesting the enhanced TG loss in *bsc2*Δ yeast required Tgl3. Since yeast also encode Tgl4 and Tgl5 TG lipases, we also performed cerulenin pulse experiments on WT, *bsc2*Δ, *tgl3*Δ*tgl4*Δ*tgl5*Δ, *bsc2*Δ*tgl3*Δ*tgl4*Δ*tgl5*Δ and measured TG before and after 3hrs of cerulenin (**Figure 2.4D**). Similarly, *tgl3*Δ*tgl4*Δ*tgl5*Δ yeast and *bsc2*Δ*tgl3*Δ*tgl4*Δ*tgl5*Δ contained near identical TG levels following 3hrs of cerulenin-induced TG lipolysis. Collectively, this supports a model where *bsc2*Δ yeast exhibit enhanced TG lipolysis that is suppressed by genetic depletion of Tgl lipase activity.

Next, we determined whether Bsc2 loss alters TG biosynthesis. We utilized a yeast strain in which all of the acyltransferases that synthesize neutral lipids were deleted, with the exception of Dga1. In this strain, the DGA1 gene was placed under a galactose inducible promoter (*are1*Δ*are2*Δ*lro1*Δ^{GAL}DGA1, referred here simply as "^{GAL}DGA1") (Cartwright et al., 2015). As expected, in the absence of galactose, this yeast strain contains no neutral lipids and no LDs, and therefore staining yeast with MDH reveals no LD foci (**Figure 2.4E, time T=0**). In the presence of galactose in the growth media, the yeast synthesize TG via Dga1 expression

and activity. We deleted *bsc2*Δ in this strain (*bsc2*Δ ^{GAL}DGA1) and compared this strain and ^{GAL}DGA1 strain's abilities to produce LDs and TG. First, we imaged LDs via MDH stain in ^{GAL}DGA1 vs *bsc2*Δ ^{GAL}DGA1 yeast at multiple timepoints after galactose induction (**Figure 2.4E**). Visually, there was no detectable difference in the appearance of MDH-stained LDs in *bsc2*Δ compared to WT yeasts, suggesting LD biogenesis was unperturbed by Bsc2 loss. Next, we measured whole-cell TG levels in the same strains following galactose induction of TG synthesis. We found no significant difference in TG levels between these strains over multiple time-points following GAL-induction (**Figure 2.4F,G**). Additionally, we detected no significant changes in free fatty acids (FFA) for either strain, although there was a slight upward trend of FFA accumulation in the *bsc2*Δ yeast after 6 hrs, potentially due to enhanced TG lipolysis (**Figure 2.4H**). Altogether, these results support a model where the decreased TG observed in *bsc2*Δ yeast is not due to decreased TG biosynthesis, but primarily due to enhanced Tgl3-dependent TG lipolysis.

The Bsc2 HR1 and HR2 regions are sufficient for Bsc2 function

Since the Bsc2 HR1 and HR2 regions appeared responsible for LD interactions, we next asked whether these regions were sufficient for Bsc2 function. We generated yeast with chromosomal GFP-tagged full length Bsc2 (Bsc2^{FL}-GFP) or truncated Bsc2 encoding only the N-terminal region, HR1, and HR2 (Bsc2$^{N\text{-}HR1+HR2}$-GFP). Both GFP-tagged strains localized to LDs, although Bsc2$^{N\text{-}HR1+HR2}$-GFP appeared more dimly localized to LDs (**Figure 2.4I**). Additionally, we tested the ability of the Bsc2$^{N\text{-}HR1+HR2}$-GFP to protect against enhanced lipolysis (**Figure 2.4J**). As expected, initial (T_0) STAT phase TG levels for Bsc2^{FL}-GFP,

Bsc2$^{N\text{-}HR1+HR2}$-GFP, and *bsc2*Δ were not significantly different (**Figure 2.4J**). However, after 3hrs of cerulenin-stimulated lipolysis (T_3), steady-state TG levels of yeast expressing Bsc2$^{N\text{-}HR1+HR2}$ were similar to WT yeast with Bsc2^{FL,} and significantly elevated compared to *bsc2*Δ yeast (**Figure 2.4J**). This suggests that the LCR region is not necessary for Bsc2 function, and that the N-HR1-HR2 region is sufficient for *in vivo* function.

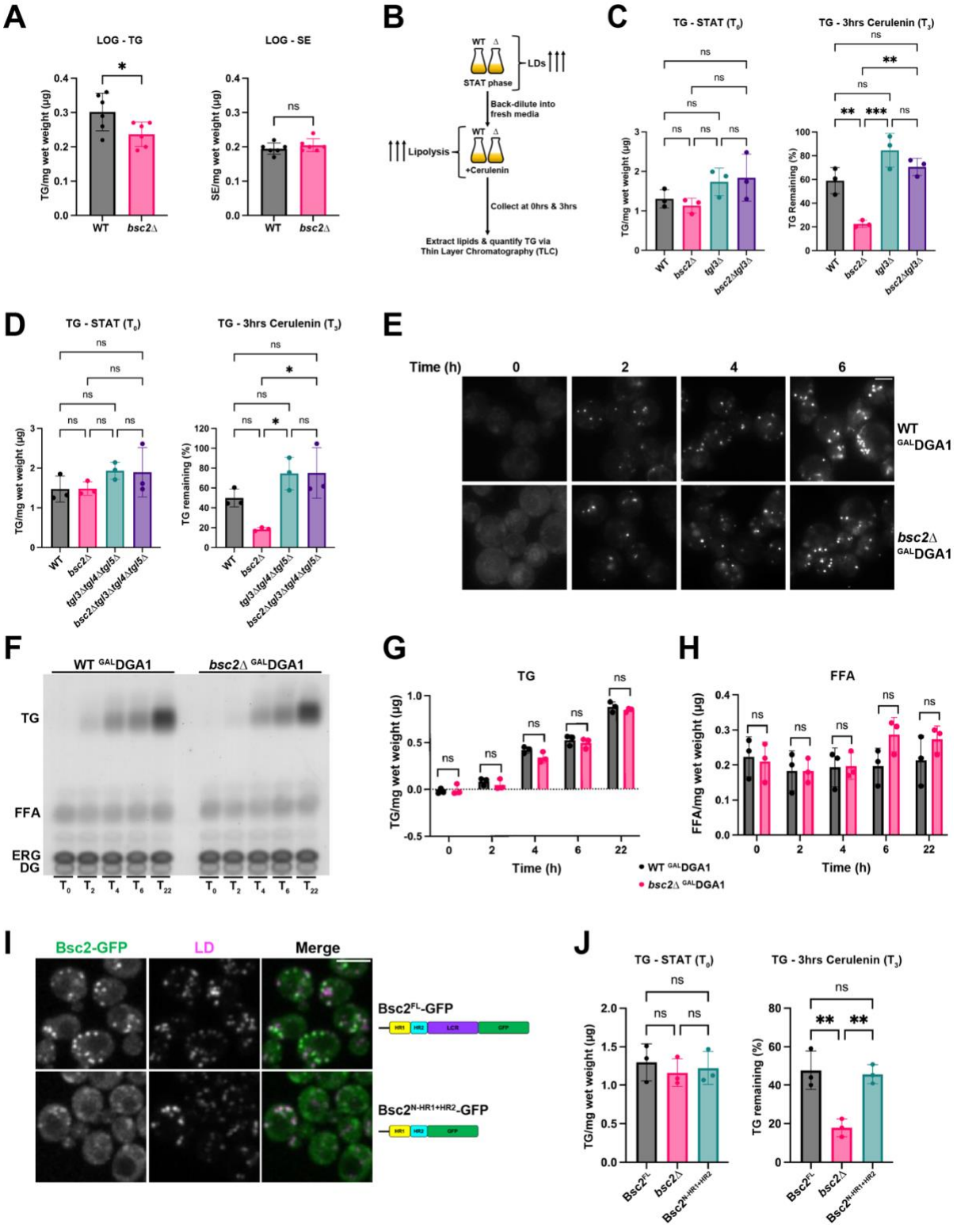
A
LOG - TG
LOG - SE
TG/mg wet weight (µg)
SE/mg wet weight (µg)
WT
bsc2Δ
B
STAT phase
LDs
Back-dilute into fresh media
Lipolysis
+Cerulenin
Collect at 0hrs & 3hrs
Extract lipids & quantify TG via Thin Layer Chromatography (TLC)
C
TG - STAT (T0)
TG - 3hrs Cerulenin (T3)
TG/mg wet weight (µg)
TG Remaining (%)
tgl3Δ
bsc2Δtgl3Δ
D
TG - STAT (T0)
TG - 3hrs Cerulenin (T3)
TG/mg wet weight (µg)
TG remaining (%)
tgl3Δtgl4Δtgl5Δ
bsc2Δtgl3Δtgl4Δtgl5Δ
E
Time (h)
0
2
4
6
WT GALDGA1
bsc2Δ GALDGA1
F
WT GALDGA1
bsc2Δ GALDGA1
TG
FFA
ERG
DG
G
TG
TG/mg wet weight (µg)
Time (h)
H
FFA
FFA/mg wet weight (µg)
Time (h)
WT GALDGA1
bsc2Δ GALDGA1
I
Bsc2-GFP
LD
Merge
Bsc2FL-GFP
Bsc2N-HR1+HR2-GFP
J
TG - STAT (T0)
TG - 3hrs Cerulenin (T3)
TG/mg wet weight (µg)
TG remaining (%)
Bsc2FL
bsc2Δ
Bsc2N-HR1+HR2

Figure 2.4. Bsc2 deletion results in enhanced Tgl3 lipase-dependent TG lipolysis

(A) Log phase, whole cell TG (left graph) and SE (right graph) levels of wildtype (WT) and *bsc2*Δ yeast, measured by TLC. Experiments conducted in triplicate. Statistical analysis is Unpaired t test with Welch's correction.

(B) Graphical schematic of cerulenin lipolysis assay for yeast.

(C) TLC quantification of STAT phase, pre-lipolysis (T_0) TG levels of WT, *bsc2*Δ, *tgl3*Δ, and *bsc2*Δ*tgl3*Δ (left panel). Rate of lipolysis determined via TLC after addition of 10µg/mL cerulenin (T_3) for these same strains (right panel). Quantification represents percentage of starting TG remaining (pre-cerulenin TG levels set to 100% for each strain) after 3hrs of cerulenin-stimulated lipolysis. Experiments conducted in triplicate. Statistical analyses are ordinary one-way ANOVA.

(D) TLC quantification of STAT phase, pre-lipolysis TG levels of WT, *bsc2*Δ, *tgl3*Δ*tgl4*Δ *tgl5*Δ, and *bsc2*Δ*tgl3*Δ*tgl4*Δ *tgl5*Δ (left panel). Rate of lipolysis determined via TLC after addition of 10µg/mL cerulenin for these same strains (right panel). Quantification represents percentage of starting TG remaining (pre-cerulenin TG levels set to 100% for each strain) after 3hrs of cerulenin-stimulated lipolysis. Experiments conducted in triplicate. Statistical analyses are ordinary one-way ANOVA.

(E) Time-lapse imaging of galactose-induced LD formation in WT ^{GAL}DGA1 and *bsc2*Δ ^{GAL}DGA1 yeast stained with MDH. Scale bar 2µm.

(F) Representative TLC plate of galactose-induced TG production in WT ^{GAL}DGA1 and *bsc2*Δ ^{GAL}DGA1 yeast strains. FFA = Free Fatty Acids, ERG = Ergosterol, DG = Diacylglyceride.

(G) TLC quantification of TG levels after galactose-induced TG production time-course in WT ^{GAL}DGA1 and *bsc2*Δ ^{GAL}DGA1. Representative of three independent experiments. Statistical analyses are multiple unpaired t tests with Welch's correction.

(H) TLC quantification of FFA levels after galactose-induced TG production time-course in WT ^{GAL}DGA1 and *bsc2*Δ ^{GAL}DGA1. Representative of three independent experiments. Statistical analyses are multiple unpaired t tests with Welch's correction.

(I) LOG phase imaging of endogenous WT full-length Bsc2-GFP (Bsc2^{FL}-GFP) and truncated Bsc2 with GFP inserted after HR2 (Bsc2$^{N\text{-}HR1+HR2}$-GFP), with MDH stained LDs. Scale bar 5µm.

(J) TLC quantification of STAT phase, pre-lipolysis TG levels of Bsc2^{FL}-GFP, *bsc2*Δ, and Bsc2$^{N\text{-}HR1+HR2}$-GFP (left panel). Rate of lipolysis determined via TLC after addition of 10µg/µL cerulenin for these same strains (right panel).

(J, continued) Quantification represents percentage of starting TG remaining (pre-cerulenin TG levels set to 100% for each strain) after 3hrs of cerulenin-stimulated lipolysis. Experiments conducted in triplicate. Statistical analyses are ordinary one-way ANOVA. *, $P < 0.05$; **, $P < 0.01$: ***. $P < 0.001$: ****. $P < 0.0001$.

Bsc2 over-expression results in TG and LD enlargement

Since Bsc2 loss appeared to enhance TG lipolysis, we next determined how Bsc2 over-expression would influence LD neutral lipids. We measured steady-state TG and SE levels of WT yeast expressing either an empty vector (EV) or over-expressed Bsc2 (Bsc2 OE) on a GPD promoter. Strikingly, we observed a more than ~4-fold increase in TG stores in Bsc2 OE yeast compared to EV controls (**Figure 2.5A**). In contrast, there was no effect on SE levels, suggesting Bsc2 OE selectively impacted TG pools (**Figure 2.5A)**. In line with this, we observed enlarged LDs in Bsc2 OE when they were imaged by thin section transmission electron microscopy (TEM) (**Figure 2.5B**). Quantification of TEM micrographs confirmed significantly increased LD sizes and numbers of detected LDs per thin-section of Bsc2 OE cells compared to WT (**Figure 2.5C,D**), suggesting Bsc2 OE elevated TG stores that were stored in enlarged LDs. A portion of the LDs observed in Bsc2 OE had similar area to those of EV LDs, which are likely explained by the varying expression levels of the Bsc2 OE construct. Collectively, this indicates that Bsc2 OE correlates with elevated TG levels and enlarged LDs.

A possible explanation for the TG accumulation in Bsc2 OE yeast is simply from over-expressing a hydrophobic LD surface protein, which could potentially crowd away other LD-resident proteins and perturb TG homeostasis (Kory et al., 2015). To test this possibility, we measured steady-state neutral lipid levels of yeast over-expressing Pln1 (also known as Pet10),

a well characterized yeast perilipin-like protein (Gao et al., 2017), and compared these to EV and Bsc2 OE expressing yeast (**Figure 2.5E**). Strikingly, Pln1 OE did not alter TG levels, which closely mirrored the EV control, and did not phenocopy the TG accumulation observed with Bsc2 OE (**Figure 2.5E**). Notably, neither of the constructs altered SE pools. This indicated that the TG and LD accumulation caused by Bsc2 OE was likely not an artifact of simply overexpressing a LD protein, and supported a model where Bsc2 OE specifically influenced LD TG levels. In support of this, Western blot analysis of Bsc2 OE and Pln1 OE expression levels revealed very similar expression levels of both proteins, suggesting they were expressing at similar high levels (**Figure 2.5F**). Collectively, this supports a model where Bsc2 influences LD TG pools, and that its over-expression is sufficient to induce TG accumulation.

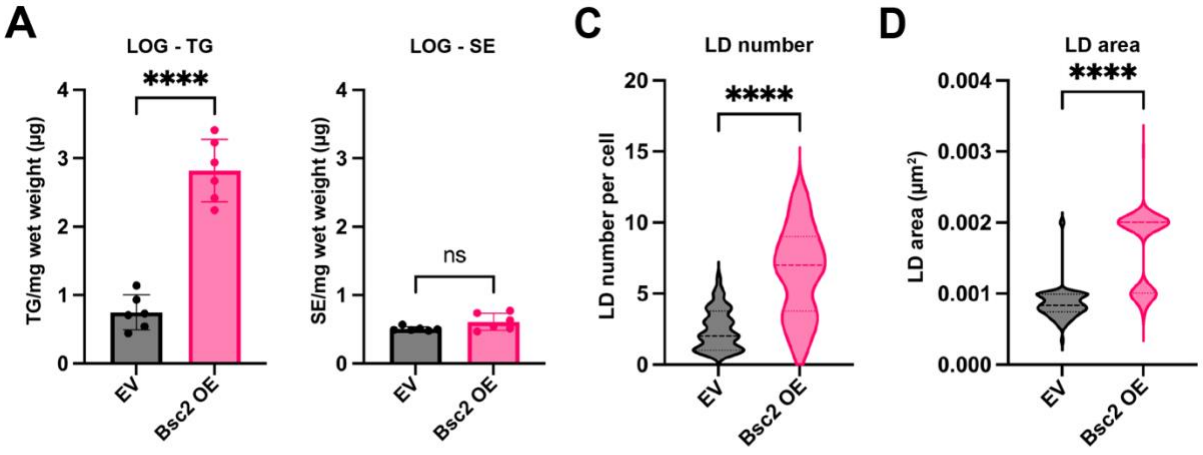
A
LOG - TG
****
TG/mg wet weight (µg)
EV
Bsc2 OE
LOG - SE
ns
SE/mg wet weight (µg)
C
LD number
****
LD number per cell
D
LD area
****
LD area (µm²)

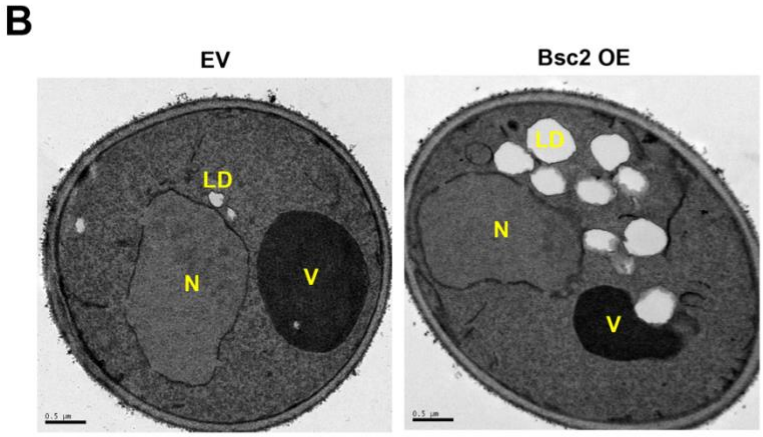
B
EV
Bsc2 OE
LD
N
V

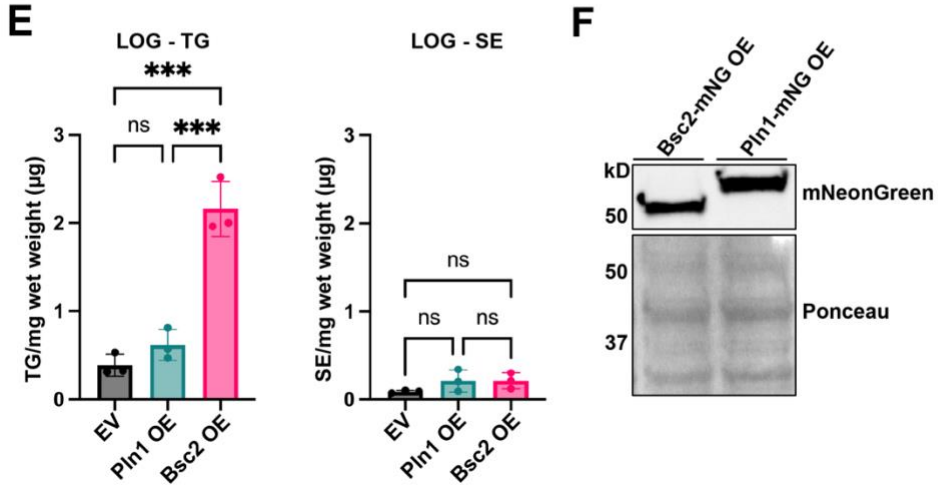
E
LOG - TG
***
ns
***
TG/mg wet weight (µg)
EV
Pln1 OE
Bsc2 OE
LOG - SE
ns
SE/mg wet weight (µg)
F
Bsc2-mNG OE
Pln1-mNG OE
kD
50
mNeonGreen
50
Ponceau
37

Figure 2.5. Overexpression of Bsc2 significantly elevates TG levels, LD number and LD size.
(A) Steady state, LOG phase, TG (left panel) and SE (right panel) levels in empty vector plus soluble GFP (EV) and Bsc2-mNeonGreen overexpressing (Bsc2 OE) yeast as quantified by TLC. Data were compiled from three independent experiments.
(B) Thin-section TEM micrographs of LOG phase EV and Bsc2 OE yeast. LD = Lipid Droplet, N = Nucleus, V = Vacuole.
(C) LD number quantification from Fig 5B micrographs. n = 44 cells for EV and n = 18 cells for Bsc2 OE.
(D) LD area quantification from Fig 5B micrographs. n = 98 LDs for EV and n = 115 LDs for Bsc2 OE.
(E) Steady state TG (left panel) and SE (right panel) levels at LOG for EV, Bsc2 OE, and Pln1 overexpressing (Pln1 OE) yeast. Experiments were performed in triplicate.
(F) Protein expression of Bsc2-mNeonGreen and Pln1-mNeonGreen overexpressing constructs used in Fig 5E. Membranes blotted with anti-mNeonGreen antibody and Ponceau S stain served as loading control for total protein. Scale bars, 0.5 μm. Statistics for Fig 5A, C, and D were unpaired t test with Welch's correction. Statistics for Fig 5E was ordinary one-way ANOVA. *, $P < 0.05$; ***, $P < 0.001$; ****, $P < 0.0001$.

Bsc2 loss or over-expression does not impact Tgl lipase abundance nor LD targeting

Next we investigated the mechanism by which Bsc2 influences TG lipolysis and fat accumulation. One possibility is that Bsc2 loss or over-expression may alter the total abundance or LD localization of TG lipases. To investigate this, we first performed fluorescence imaging of GFP-tagged TG lipases Tgl3, Tgl4, and Tgl5 in WT and *bsc2*Δ yeast (**Figure 2.6A**). Imaging revealed there were no obvious changes in Tgl lipase LD targeting in the absence of Bsc2, suggesting Tgl LD targeting was intact in *bsc2*Δ yeast. We then examined steady-state Tgl protein levels by Western blotting GFP-tagged endogenous Tgl proteins. Steady-state protein abundances of Tgl3, Tgl4, and Tgl5 were unaffected by Bsc2 loss, indicating the enhanced lipolysis observed in *bsc2*Δ yeast was not simply due to increased total lipase abundances (**Figure 2.6B**).

Since Bsc2 OE led to TG accumulation, we also imaged GFP-tagged Tgl proteins in WT yeast and yeast over-expressing an untagged Bsc2. As expected, yeast over-expressing

Bsc2 displayed larger and more numerous LDs, but this did not alter the LD localization of any of the GFP-tagged Tgl proteins, suggesting Bsc2 OE does not inhibit their LD targeting (**Figure 2.6C**). Similarly, Western blotting revealed the abundances of Tgl lipases were unchanged in Bsc2 OE compared to WT, indicating that the TG accumulation in Bsc2 OE was not due to decreased lipase expression (**Figure 2.6D**). Collectively, this indicates that changes in steady-state TG levels in *bsc2*Δ or Bsc2 OE are not due to perturbations in the abundances of TG lipases nor their LD targeting.

To determine whether Bsc2 may physically interact with Tgl lipases on the LD surface, we also conduced co-immunoprecipitation (co-IP) experiments where we over-expressed either mNG (EV-mNG) alone or Bsc2-mNG in yeast, immunoprecipitated with anti:mNG affinity resin, and examined the co-IP fractions by LC-MS/MS proteomics. Notably, numerous canonical LD proteins were significantly enriched in the Bsc2-mNG co-IP fraction, including Erg6, Hfd1, Faa1, and Eht1 (**Figure 2.6G**). However, we did not detect any peptides from Tgl3, Tgl4, nor Tgl5 in this experiment. While we cannot rule out that Bsc2 and Tgl lipases interact, this indicates that Bsc2 may not form functionally significant interactions with Tgl lipases.

Bsc2 and Tgl3 independently target to LD subsets

Since Bsc2 manipulation did not appear to influence Tgl3 (or any Tgl lipase) abundance or localization, we hypothesized that Bsc2 may demarcate a subset of TG-positive LDs, and interact with the TG pool there independently of Tgl lipases. If Tgl3 were to also target this Bsc2-positive LD pool, it could in principle directly compete with Bsc2 for TG access on the

monolayer surface. In this model, Bsc2 may function as a negative regulator of TG lipolysis through stochastic competition for TG. If so, then depletion of Bsc2 would result in elevated lipolysis, and Bsc2 over-expression would promote TG accumulation. In support of this model, MD simulations indicated that Bsc2 strongly interacted with TG in model LDs (**Figure 2.3**).

To test this model, we directly compared Bsc2 and Tgl3 LD localizations in yeast co-expressing chromosomally tagged Bsc2-GFP and Tgl3-mRuby. Prior to cerulenin treatment (T_0), we observed LDs with detectable levels of both Bsc2-GFP and Tgl3-mRuby (**Figure 2.6E, yellow arrows**), as well as LDs exhibiting only detectable Bsc2-GFP (**Figure 2.6E, green arrows**) or Tgl3-mRuby alone (**Figure 2.6E, red arrows**). This indicated that Bsc2 and Tgl3 can occupy the same LD, but also distinct LD subsets within a cell, suggesting they target to LDs independently of one another.

Next, we imaged these same dual-labeled yeast following 3hrs (T_3) of cerulenin treatment to induce lipolysis (**Figure 2.6E**). We then quantified LDs for Bsc2-GFP and Tgl3-mRuby signal above background, and generated signal correlation graphs (**Figure 2.6F**). Notably, at T_0 there is a heterogenous mix of Bsc2-GFP and Tgl3-mRuby signals on LDs, with some LDs displaying abundant Tgl3-mRuby signal but low Bsc2-GFP signal (Tgl3>Bsc2, upper-left region of chart, red circle), LDs with significant levels of both Bsc2-GFP and Tgl3-mRuby signals (Tgl3~Bsc2, center to upper-right region of chart), and LDs with high Bsc2-GFP but low Tgl3-mRuby signal (Bsc2>Tgl3, lower right region of chart). In line with this, the Pearson correlation was relatively low, r=0.3701. This variation of Bsc2-to-Tgl3 signal supports a model where these two proteins independently target to LDs.

Following 3hrs of cerulenin treatment, the Bsc2-GFP/Tgl3-mRuby LD signal distribution changed. LDs now displayed a more linear positive correlation pattern, with Bsc2-GFP signal correlating with Tgl3-mRuby signal (i.e., Tgl3/Bsc2), and a Pearson correlation of r=0.8774 (**Figure 2.6F, red circle**). Collectively, this supports a model where LDs with detectable Tgl3, but low or undetectable Bsc2, may be depleted or altered during TG lipolysis, whereas LDs with more abundant Bsc2-GFP are retained following 3hrs cerulenin-induced TG lipolysis.

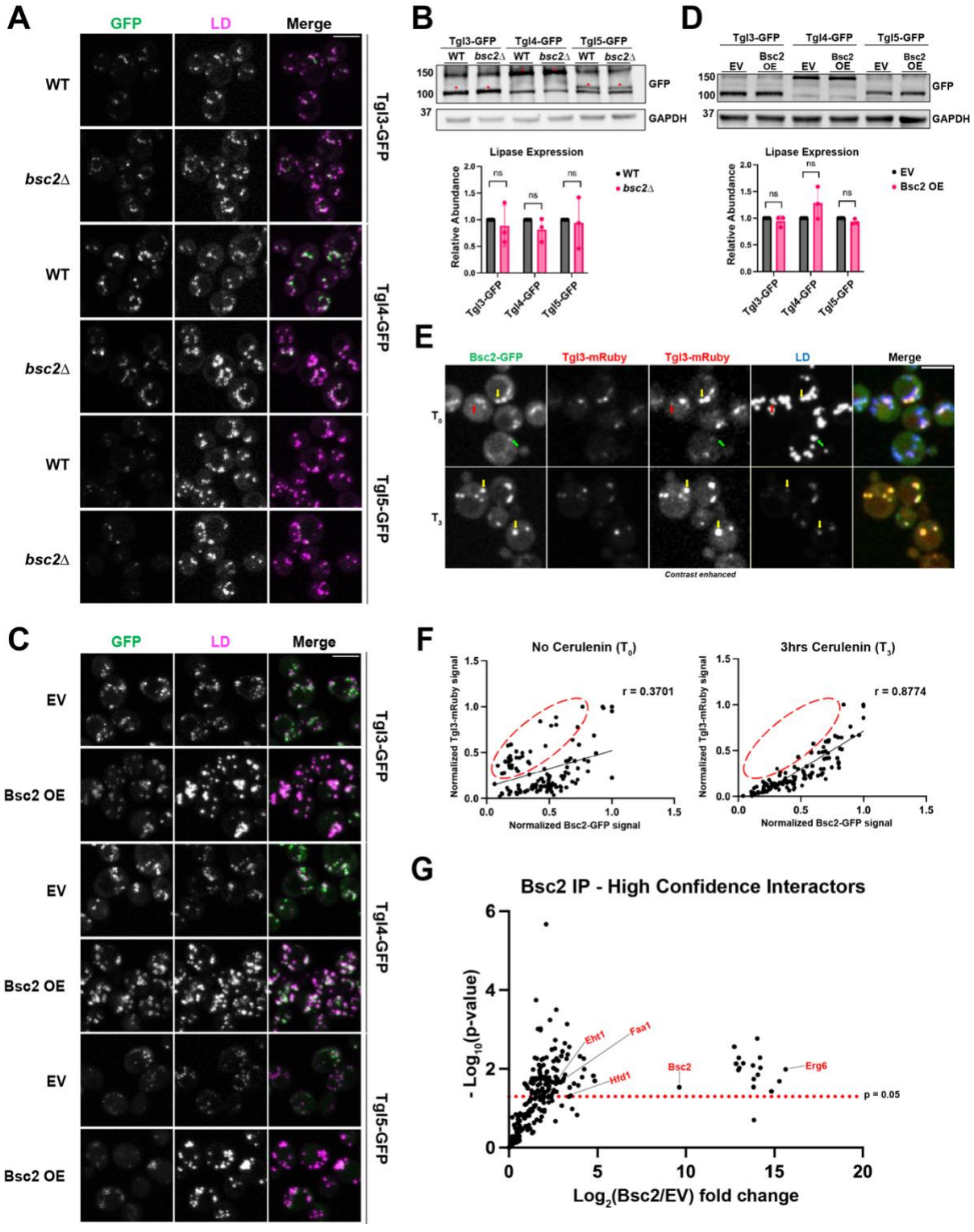
A
GFP
LD
Merge
WT
bsc2Δ
Tgl3-GFP
Tgl4-GFP
Tgl5-GFP
B
Tgl3-GFP
Tgl4-GFP
Tgl5-GFP
WT
bsc2Δ
150
100
37
GFP
GAPDH
Lipase Expression
Relative Abundance
ns
WT
bsc2Δ
D
EV
Bsc2 OE
E
Bsc2-GFP
Tgl3-mRuby
LD
Merge
T0
T3
Contrast enhanced
C
Bsc2 OE
F
No Cerulenin (T0)
3hrs Cerulenin (T3)
r = 0.3701
r = 0.8774
Normalized Tgl3-mRuby signal
Normalized Bsc2-GFP signal
G
Bsc2 IP - High Confidence Interactors
- Log10(p-value)
Log2(Bsc2/EV) fold change
Eht1
Faa1
Hfd1
Bsc2
Erg6
p = 0.05

Figure 2.6. Bsc2 does not alter TG lipase LD-targeting or protein abundance, but modulates lipolysis on the LD.
(A,C) Fluorescence imaging of GFP-tagged TG lipases in either WT and *bsc2*Δ (A) or EV and untagged Bsc2 OE yeast (C). LDs were stained with MDH.
(B,D) Protein expression levels of GFP-tagged TG lipases in WT and *bsc2*Δ (B) and EV and Bsc2 OE (D). Red asterisks indicated GFP-tagged lipases. Data is normalized to WT or EV, respectively, and represents three independent experiments.
(E) Fluorescence imaging of Bsc2-GFP and Tgl3-mRuby dual-tagged yeast, with MDH stained LDs before (T_0) and 3hrs after cerulenin-stimulated lipolysis (T_3). Green arrows indicate Bsc2-enriched LDs, red arrows indicate Tgl3-enriched LDs, and yellow arrows indicate LDs targeted with both Bsc2 and Tgl3. Second from left column represents non-contrast adjusted images for Tgl3-mRuby.
(F) Scatterplot of Bsc2-GFP fluorescence signal intensity versus Tgl3-mRuby signal intensity for random LDs before (T_0) and after 3hrs cerulenin treatment (T_3) with Pearson's correlation coefficient (r) displayed. Data corresponding to images in Fig 6E. Red circles indicate Tgl3-enriched/Bsc2-deenriched LDs. n = 120 LDs for each condition, quantified from 87 cells for T_0 and 105 cells for T_3.
(G) Volcano plot showing negative Log_{10} P value (- Log_{10}) and Log_2 abundance changes for Bsc2 IP interactors versus EV control, obtained via mass spec analysis. Red text at select data points indicates LD proteins found to directly interact with Bsc2. Red dotted line indicates significance cut-off for protein hits. Data were collected from three independent experiments. Statistical analyses are multiple unpaired t tests. Scale bars are 5μm. ns, ≥ 0.05.

Bsc2 loss alters LD accumulation in yeast stationary phase

As yeast transition into STAT phase, they enter slow growth and shunt excess lipids into TG for long-term storage. Since Bsc2 loss elevated TG lipolysis, we queried whether *bsc2*Δ yeast would display differences in LD abundances as they transitioned into long-term STAT phase. We quantified the number of LDs per yeast cell for WT and *bsc2*Δ yeast initially cultured in 2% glucose media and allowed to grow continually in this media for six days (defined as gradual glucose restriction, GGR). At the start of the experiment (T=0 days), when cells were in early STAT phase, *bsc2*Δ yeast exhibited more MDH-stained LDs compared to WT (**Figure 2.7A,B**). However, following six days of GGR, *bsc2*Δ yeast displayed significantly fewer LDs per cell than WT yeast (**Figure 2.7A,B**). This supports a model where Bsc2 depletion causes elevated TG lipolysis, which over time would gradually deplete LD

stores in yeast subsisting in long-term low-nutrient conditions. Collectively, we propose a model in which Bsc2 labels a subset of TG-containing LDs and marks them for preservation from lipolysis, which could in principle be utilized as a lipid source in stationary phase subsistence (**Figure 2.7C**).

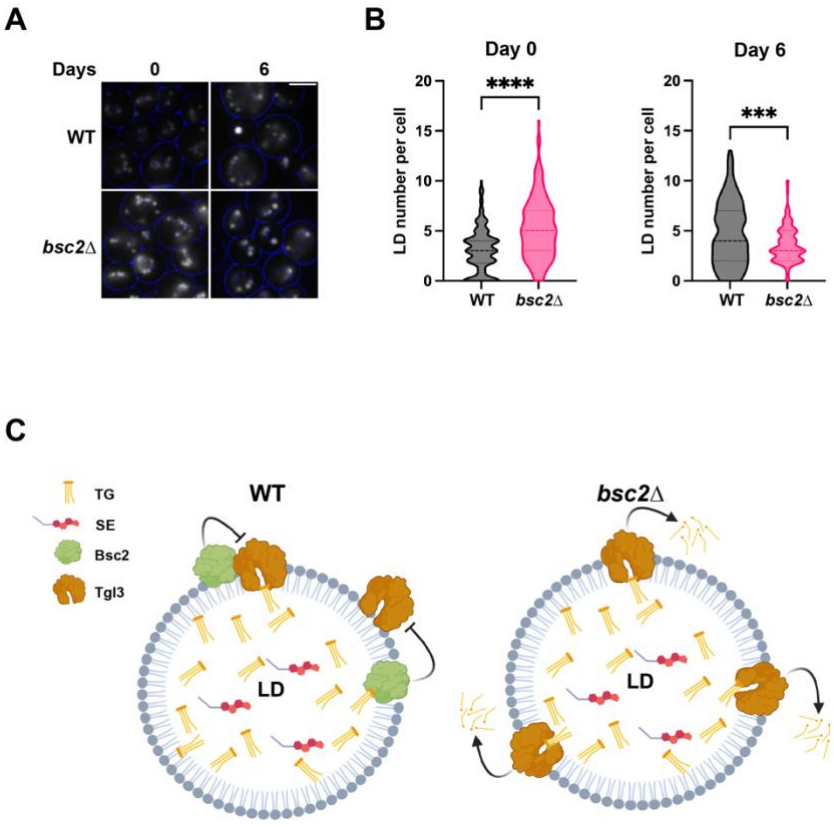

Figure 2.7. Bsc2 influences LD maintenance during late starvation conditions.
(A) Imaging of MDH-stained WT and *bsc2*Δ yeast LDs, before (Day 0) and after (Day 6) exposure to late STAT phase, also known as Gradual Glucose Restriction (GGR). Blue circles indicate cell borders.
(B) Quantification of LD number per cell at Day 0 and Day 6 of exposure to GGR, from images in Fig 7A. n = 150 cells for both WT and *bsc2*Δ, each.
(C) Cartoon model of Bsc2 negative regulation of Tgl3-dependent TG lipolysis via competition for TG substrate binding or direct interaction (WT LD, left). In the absence of Bsc2, TG is more accessible to Tgl3 lipase (*bsc2*Δ LD, right). Statistics are unpaired t test with Welch's correction. Scale bars, 5μm. **, $P < 0.01$; ****, $P < 0.0001$.

Discussion

Emerging work indicates that LDs can be classified into distinct subpopulations within single cells, and such LD subsets are differentiated by unique proteomes, morphologies, or spatial distributions (Thiam and Beller, 2017; Eisenberg-Bord et al., 2018; Teixeira et al., 2018; Schott et al., 2019; Ugrankar et al., 2019). A key knowledge gap is how distinct proteomes confer specific functions to LD subpopulations. Here, we demonstrate that Bsc2 is a yeast protein with amphipathic and hydrophobic regions that enriches on a subpopulation of LDs and acts as negative regulator of TG lipolysis. We also find that Bsc2 LD targeting requires TG, and MD simulations reveal that Bsc2 hydrophobic regions adopt specific conformations on TG-rich LDs and engage in extensive interactions with TG. Loss of Bsc2 reduces steady state TG levels at LOG growth phase (but does not alter SE pools), and we find this is due to enhanced lipolysis and not by decreased TG synthesis. Bsc2 over-expression accumulates whole-cell TG and enlarged LDs, a phenotype not replicated by overexpressing another hydrophobic LD coat protein Pln1/Pet10. We hypothesize this is due to a Bsc2-dependent block in lipolysis, though this does not exclude other changes such as elevated TG synthesis or LD biogenesis as contributing factors. We also find that yeast lacking Bsc2 display altered LD mobilization in late-phase STAT phase. This may indicate that in the absence of Bsc2, lipolysis in STAT phase is dysregulated and LDs are differentially mobilized, supporting a model where Bsc2 helps maintain a LD subset for longer-term subsistence.

A pervasive question in LD biology is how proteins target to LDs. One factor that clearly influences both LD protein targeting and stability is the presence of neutral lipids in

LDs (Grillitsch et al., 2011; Schmidt et al., 2013; Klein et al., 2016; Gao et al., 2017; Prévost et al., 2018; Chorlay and Thiam, 2020; Rogers et al., 2022). Our Bsc2 structure-function analysis indicate that both HR1 and HR2 contribute to organelle targeting. In line with this, MD simulations indicate that HR1 and HR2 undergo significant conformation changes in response to different lipid environments. On LDs, HR2 adopts a more compact helix-kink-helix conformation and interacts with TG, in contrast to a more "splayed open" conformation in the ER bilayer. HR1 also interacts extensively with TG and PLs on the LD surface, but disengages entirely from the SE-rich LD surface. This indicates that both HR1 and HR2 may enable Bsc2 to anchor on LDs, but HR1 may act as a LD "compositional sensor", preferentially engaging TG-rich LDs and potentially explaining why Bsc2 is detected on only LD subsets that may have more accessible TG *in vivo*. In the absence of TG, Bsc2 may adopt a less favorable conformation and be targeted for degradation, although further studies are needed for confirmation. This may explain why Bsc2 LD targeting is significantly less detectable in SE-only yeast.

How does Bsc2 regulate TG lipolysis? We show that Bsc2 loss or over-expression does not alter Tgl lipase LD targeting nor protein abundance, and co-IP mass spectrometry analysis indicated that Bsc2 does not detectably interact with Tgl3. This collectively suggests that Bsc2 is likely not a strong interactor with Tgl lipases, and therefore does not likely regulate lipolysis through strong direct enzyme interactions. An alternative hypothesis is that Bsc2 competes with Tgl3 for TG-binding on the LD surface by occupying lipid packing defects, effectively altering TG substrate availability and prohibiting Tgl lipases from mobilizing TG.

Previous visual screens have identified a number of yeast proteins that target LD subpopulations and aid in the formation and maintenance of specific LD subsets. The most studied examples are the isoforms Ldo16 and Ldo45, which demarcate a specific pool of LDs formed near the yeast nucleus-vacuole junction, and are determinants of the targeting of other LD proteins, such as Pdr16, to these spatially distinct LDs (Eisenberg-Bord et al., 2018; Teixeira et al., 2018; Ren et al., 2014). During their investigation into Ldo45/Ldo16 function, Eisenberg-Bord et al also identified Bsc2 as a marker of the Pdr16-enriched LD subset (Eisenberg-Bord et al., 2018). Our study now characterizes Bsc2 as a regulator of TG lipolysis, as well as provides a working model for how it localizes to a subset of TG-rich LDs. In the future, we hope to further reveal the function of this Bsc2-positive LD subset in yeast physiology and metabolic adaptation.

CHAPTER THREE

Materials and Methods

Yeast strains and growth conditions

The WT parental strain used for all experiments and cloning in this study was BY4741 (MATa *his3*Δ1 *leu2*Δ0 *met15*Δ0 *ura3*Δ0). W303-1A (MATa leu2-3, 112 trp1-1 can1-100 ura3-1 ade2-1 his3-11,14) yeast strain was used as the parental strain for imaging of yeast with different neutral lipid-containing backgrounds (Figure 1E) and for galactose induced TG synthesis experiments (Figure 4E-H). Synthetic-complete (SC) growth media was used for culturing yeast cells in all experiments, except for experiments where uracil was excluded to retain pBP73G or pRS316 plasmids. For all experiments (unless noted below), a colony of yeast was inoculated from a YPD (yeast extract peptone dextrose) plate into SCD (SC dextrose/glucose) media and allowed to grow for ~ 24hr in a 30°C incubator with shaking at 210 rpm. These cultures were diluted to OD_{600} = 0.001 in SCD media containing 2% glucose (wt/vol), grown overnight in a 30˚C incubator shaking at 210 rpm, and collected at mid-log phase (~OD_{600} = 0.6) the next day. For cerulenin experiments, yeast were cut back to OD_{600} = 0.1 in SCD media from an overnight culture and grown for 24hr, 30˚C, 210 RPM. 50 OD_{600} units were collected from the 24hr culture as pre-lipolysis sample (Time 0hrs, "T_0"). The remainder of the 24hr culture was cut back to OD_{600} = 0.5 in fresh SCD media containing 10µg/mL Cerulenin (Cat# C2389; Sigma-Aldrich) final concentration and allowed to incubate for 3hrs before harvesting 50 OD_{600} units as a post-lipolysis sample (Time 3hrs, "T_3"). Aliquots were then washed in MiliQ water, pelleted, and then processed for lipid extraction and TLC. Culturing of yeast for

cerulenin imaging experiments (Figure 5E) was done as detailed above, except a small aliquot was removed from 24hr culture as T_0 and ~25 OD_{600} was removed at T_3 from SCD plus Cerulenin cultures. All samples were concentrated down to 1mL in their respective media, and LDs stained for 5 min with MDH (SM1000a; Abcepta) at a final concentration of 0.1 mM before imaging. For induction of TG synthesis, ^{GAL}DGA1 yeast strains were first cultured in 0.2% dextrose SCD media, overnight. Cells were then pelleted, washed in MiliQ water, and resuspended in 2% raffinose SCR media (2% raffinose substituted for dextrose in SCD) at OD_{600} = 0.5 and cultured for 24hrs. Following 24hr incubation, 50 OD_{600} units were removed as Time 0 ("T_0") sample for lipid extraction and TLC. The remainder of the yeast were pelleted, washed in MiliQ water, then cut back to OD_{600} = 2 in SCG media (2% galactose substituted for dextrose in SCD), and incubated for 22hrs. 50 OD_{600} unit aliquots were removed at 2, 4, 6, and 22hrs incubation, washed in Mili-Q water, then pelleted and processed for lipid extraction and TLC. For imaging of induced LDs, ^{GAL}DGA1 yeast strains were cultured same as above, except 1mL aliquots were taken from SCG cultures at indicated time points and incubated for 5 min with MDH at a final concentration of 0.1 mM to visualize LDs. For gradual glucose restriction LD imaging experiments, yeast were cultured from a plate overnight in SCD media. 1mL of overnight culture was taken for Day 0, stained with MDH and LDs were imaged. The remainder of the culture was cut back to OD_{600} = 0.1 in fresh SCD media and incubated for 6 days, with 1mL aliquots taken each day and LDs imaged after staining with MDH. For immunoprecipitation and proteomics, cells were cultured from plates into SCD-URA (without uracil) overnight. Then, yeast were cut back to OD_{600} = 0.1 into same drop-out media, then incubated for 24hrs (under general growth conditions described above) until they reached

stationary phase. After 24hrs, 250 OD_{600} units were collected for each sample, pelleted at 4000 RPM for 5 min, washed in Mili-Q water then pelleted again. Final yeast pellets were then subjected for protein extraction and immunoprecipitation.

Molecular Dynamics Simulations

Structure prediction: TOPCONS (Tsirigos et al., 2015) and TmAlphaFold (Dobson et al., 2023) were used to predict the membrane-embedded regions of Bsc2. The protein structure prediction tools RoseTTAFold (Baek et al., 2021) and AlphaFold2 (Jumper et al., 2021) were then used to model the structure of $Bsc2^{N\text{-}HR1+HR2}$ (amino acids 1-100). The resulting output poses from both resources agreed on the placement and alignment of all helices within the protein. This included HR1 in a single amphipathic helical structure and HR2 in a helix-kink-helix structure. The final structure was taken from RoseTTAFold, using no pairing or templates. Notably, the 5 top-scoring structures from RoseTTAFold had quite similar alignment. The output for TOPCONS transmembrane topology and the selected final structure are in Figureures S3M and S3C, respectively.

Simulations: The CHARMM36 force field (Campomanes et al., 2021), (Klauda et al., 2010) was used in all simulations. The bilayer system was created in the CHARMM-GUI membrane builder (Jo et al., 2008) with a ratio of 88:37:10 ratio of 3-palmitoyl-2-oleoyl-D-glycero-1-phosphatidylcholine (POPC), 2,3-dioleoyl-D-glycero-1-phosphatidylethanolamine (DOPE), and phosphatidylinositol (SAPI), respectively. This corresponds to 135 PLs per leaflet (270 PLs total per system). The LD systems had the same membrane compositions for their respective monolayer leaflets and included an 8 nm thick neutral lipid core composed of a

90:10 CHYO:TG ratio for the SE-rich LD and a pure-TG core for the TG-rich LD. These LD structures were taken from the last frame of 8 μs long simulations conducted in our previous work, which importantly had already obtained the properly equilibrated distributions (Braun and Swanson, 2022). The membrane systems were embedded in 5nm of water and 0.15M NaCl on top and bottom to account for proper hydration and physiological conditions. To insert the Bsc2 structure into the membrane systems, in-house MDAnalysis (Gowers et al., 2016) scripting was used, placing HR2 into the bilayer and LD monolayers and HR1 0.5 nm above the membrane. Overlapping PLs and neutral lipids were removed and the systems were minimized for 5000 steps before being re-equilibrated for 10 ns using NVT conditions and 100 ns using NPT conditions. For the bilayer and TG-LD systems, long-timescale simulations lasting 4.5 μs were conducted using the Anton2 supercomputer provided by Pittsburg Supercomputing Center (Shaw et al., 2014), while the 90:10 CHYO:TG system was run for 1 μs on the EXPANSE supercomputer provided by San Diego Supercomputing Center (Strande et al., 2021). The simulations were conducted using a 2.4 fs timestep in the Anton2 simulations, and a 2 fs timestep in the EXPANSE simulation. The temperatures were all set to 310 K, using Nose-Hoover thermostat **(Nosé, 1984)**,(Hoover, 1985) and a temperature coupling time constant of 1 ps. The particle mesh Ewald (PME) algorithm (Essmann et al., 1995) was used to calculate the long-range electrostatic interactions with a cutoff of 1.0 nm. Lennard–Jones pair interactions were cutoff at 12 Å with a force-switching function between 8 and 12 Å, and pressure was maintained semi-isotropically using the Parrinello-Rahman barostat (Parrinello and Rahman, 1981). The pressure was set to 1.0 bar, with a compressibility of, $4 \times 10^{-5}\ bar^{-1}$, and a coupling constant of 5.0 ps. The hydrogen bonds were constrained with

the LINCS algorithm (Hess, 2008). We calculated the coordination numbers, RDFs, and protein positions using MDAnalysis, and in-house Python scripting, and Gromacs tools (Abraham et al., 2015), and the images were rendered using Visual Molecular Dynamics (VMD) (Humphrey et al., 1996).

Metadynamics: Potentials of mean force (PMFs) for single amino acids permeating through a bilayer were conducted using Well-Tempered Metadynamics (Barducci et al., 2008) biasing the *z*-component connecting the center of mass of the membrane and the center of mass of the amino acid. The bilayers used for the metadynamics simulations were created from same initial systems described above. The system was hydrated 5 nm of water surrounding each side with 0.15 M NaCl, and the respective amino acid was placed 2 nm above the membrane surface. The amino acids included in our simulations were Phe, Gln, Leu, Ser. The amino acids were neutralized by patching with the NH2 (CT2) group at the C-terminus, and an acetyl (ACE) at the N-terminus. Four replicas of each amino acid system were run for 500 ns each. The final PMF was obtained by averaging the PMFs obtained from the four simulations. The Gaussian function was deposited every 2 ps with a height of 0.05 kJ/mol and the bias factor was set to 15. Simulations were conducted in the canonical ensemble (NVT) at a temperature of 310K, using the Gromacs version 2019.4 (Abraham et al., 2015) patched with PLUMED version 2.5.3 (Tribello et al., 2014).

Lipid extraction and TLC

For lipid extraction, 50 OD_{600} units of cells were collected for each sample, and pellet wet weights were normalized and recorded prior to extraction. Lipid extraction was performed

using a modified Folch method (Folch et al., 1957). Briefly, cell pellets were resuspended in Milli-Q water with 0.5-mm glass beads (Cat # G8772-500G; Milipore Sigma) and lysed by three 1-min cycles on a MiniBeadBeater. Chloroform and methanol were added to the lysate to achieve a 2:1:1 chloroform:methanol:water ratio. Samples were vortexed, centrifuged to separate the organic solvent and aqueous phases, and the organic solvent phase was collected. Extraction was repeated a total of three times. The organic solvent phases were combined and washed twice with 1 ml 1.0 M KCl. Prior to TLC, lipid samples were dried under a stream of argon gas and resuspended in 1:1 chloroform:methanol to a final concentration corresponding to 4 µl of solvent per 1 mg cell pellet wet weight. Isolated lipids were spotted onto heated glass-backed silica gel 60 plates (1057210001; Millipore Sigma), and neutral lipids were separated in a mobile phase of 80:20:1 hexane:diethyl ether:glacial acetic acid. TLC bands were visualized by spraying dried plates with cupric acetate in 8% phosphoric acid and baking at 145°C for an hour.

TLC quantification

Stained TLC plates were scanned and then processed for quantification using Fiji (ImageJ). Each plate was spotted with a neutral lipid reference standard mixture (Cat # 18-5C; Nu-Chek Prep). The standard was prepared in chloroform to a final concentration of 10 mg/ml and diluted to 1µg/µL before loading onto plate. The neutral lipid standard was used to create a standard curve in which the x-axis displayed the calculated lipid mass in micrograms, and the y-axis displayed the band intensity estimated by using Fiji.

LD number and area quantification

For Figure 2.5B TEM images, LDs were counted by hand using the Fiji multipoint tool. The area of these same LDs was determined by tracing the perimeter of each by hand using the Fiji freehand line tool. Each LD was selected as an ROI, then the area quantified using the "Measure" tool in Fiji and reported in μm^2. For fluorescence images in Figure 2.7A, LD number per cell was quantified by counting MDH-stained LDs, by hand, using the Fiji multipoint tool.

Fluorescent signal quantification of Bsc2 and Tgl3 imaging under cerulenin treatment

In Figure 2.6F, fluorescent signals for Bsc2-GFP and Tgl3-mRuby foci were quantified from confocal maximal projections from Figure 6E imaging using Fiji. To summarize, for each image, the midplane z-section of the DAPI channel (MDH-stained LDs) was converted to grayscale, then random LDs were selected using the oval selection tool. Each of these LDs were marked as individual ROIs, along with a random area with no fluorescent signal selected as background, then all were saved to the ROI manager. Next, the maximal projections for the DAPI, RFP, and GFP channels were merged into one image, and the previously selected LD ROIs were overlaid on to image. The fluorescent signal for each channel, represented as Raw Integrated Density, was then measured for each ROI. These values were then subtracted from the background ROI integrated density for each channel to obtain a Bsc2-GFP and Tgl3-mRuby signal value for each ROI. Then, for both GFP and mRuby channels, each ROI signal measurement was divided by the ROI with highest Raw Integrated Density to obtain a ratio (Raw Integrated Density / Max Integrated Density). For each ROI, said ratio for Bsc2-GFP

signal and Tgl3-mRuby signal were plotted against each other for “No Cerulenin” and “3hr Cerulenin” conditions. Pearson’s correlation coefficient (r) was calculated for both graphs.

Statistical analysis

Graphpad Prism 8 software was used to perform all statistical analyses, with graphs indicating the mean + standard deviation. Two-tailed, unpaired t tests were performed with Welch’s correction. Where indicated, ordinary one-way ANOVA tests were performed, with Tukey’s multiple comparisons test applied. For both t tests and ANOVA, ns, $P \geq 0.05$; *, $P < 0.05$; **, $P < 0.01$; ***, $P < 0.001$; ****, $P < 0.0001$.

Conventional TEM

Yeast cells were grown in the desired conditions and processed in the University of Texas Southwestern Electron Microscopy Core Facility using a adapted protocol from Wright (Wright, 2000). In brief, cells were fixed in potassium permanganate, dehydrated, and stained in uranyl acetate and embedded in Spurr Resin. Specimen blocks were polymerized at 60°C overnight and sectioned at 70 nm with a diamond knife (Diatome) on a Leica Ultracut UCT 6 ultramicrotome (Leica Microsystems). Sections were poststained with 2% uranyl acetate in water and lead citrate. Sections were placed on copper grids (Thermo Fisher Scientific). Images were acquired on a Tecnai G2 spirit TEM (FEI) equipped with a LaB6 source at 120 kV by using a Gatan Ultrascan charge-coupled device camera.

Whole cell protein extraction and sample preparation

Whole cell protein extracts were isolated from 25 OD_{600} units of cells. Pellet wet weights were normalized prior to freezing at −20°C. Frozen cell pellets were incubated with 20% trichloroacetic acid (TCA) for 30 min on ice with occasional mixing using a vortex. Precipitated proteins were pelleted in a 4°C centrifuge at 16,000 g for 5 min. After removing the supernatant, the pellet was washed three times with cold 100% acetone followed by brief sonication. After the washes, the protein pellets were dried in an RT speed vac for 15 min to remove residual acetone. Dried protein pellets were neutralized with 1.5M Tris-HCl pH 8.8, then resuspended directly in 250µL of 1X Laemelli sample buffer (Laemmli, 1970). Samples were briefly sonicated and boiled at 95˚C for 5 min. Figure 5F protein samples (Bsc2-mNG OE and Pln1-mNG OE) were extracted as described above, except following neutralization, protein pellets were resuspended in 250µL resuspension buffer (50mM Tris pH 6.8, 1mM EDTA, 1% SDS; 6M Urea, 1X Halt Protease and Phosphatase Inhibitor Cocktail [78441; Thermo Fisher Scientific], and 1% beta-mercaptoethanol). These samples were sonicated briefly, but not subjected to heating/boiling to prevent aggregation of these hydrophobic droplet proteins. 2X Laemelli sample buffer was added to these samples immediately prior to gel loading.

Immunoblot analysis

Following protein extraction, samples were pelleted at 16,000 g for 3 min to remove insoluble debris. Equal volumes of each sample were then subjected to SDS-PAGE and western blot analysis. Proteins were separated on a precast Mini-PROTEAN® TGX™ 10% SDS-PAGE gel (4561034; BioRad) and then transferred to a 0.45 µm nitrocellulose membrane in Towbin SDS

transfer buffer (25 mM Tris, 192 mM glycine, 20% methanol, and 0.05% SDS; pH 8.2) using a Criterion tank blotter with plate electrodes (1704070; BioRad) set to 70V constant, for 1hr. Immediately after transfer, membranes were stained with PonceauS, imaged on a ChemiDoc™ Touch Gel Imager (1708370; BioRad) and cut using a clean razor blade. Membranes were blocked with 5% milk dissolved in Tris-buffered saline +Tween (TBS-T) buffer, and primary antibodies were allowed to bind overnight at 4°C. Primary antibodies used for determining protein expression are as follows: GFP (ab290; 1:5,000 dilution; Abcam), GAPDH (ab9485; 1:2,500 dilution; Abcam), mNeonGreen (Cat# 32f6; 1:1,000 dilution; ChromoTek). Immunoblots were developed by binding HRP-conjugated anti-rabbit IgG (ab6721;1:5,000; Abcam) or anti-mouse IgG (ab6728; 1:1,000; Abcam) secondary antibodies to the membrane for 1 h in the presence of 5% milk followed by four washes in TBS-T and developing with ECL substrate (1705061; BioRad). Blot signal was captured using the same BioRad ChemiDoc™ Touch Gel Imager, as noted above. Protein expression levels were quantified by measuring band intensity using ImageJ and normalizing these values to wildtype to generate an abundance value relative to control.

Whole cell protein extraction for immunoprecipitation

Yeast were collected and prepared as described above. The samples were subjected to a modified cold glass bead cell lysis and protein extraction protocol (DeCaprio and Kohl, 2020). In brief, cells were washed in cold tris-buffered saline and pelleted at 2000 g for 5 min at 4˚C. Yeast pellets were resuspended in ice-cold lysis buffer plus protease inhibitors (50mM Tris-HCl pH 7.5, 120mM KCl, 5mM EDTA, 0.1% Nonidet P-40 Substitute, 10% Glycerol, 1mM

DTT, 1mM PMSF, and 1X Halt Protease and Phosphatase Inhibitor Cocktail [78441; Thermo Fisher Scientific]), transferred to a 2 mL screw-cap microcentrifuge tube (Cat # 02-681-343; Fisher Scientific) containing glass beads (Cat # G8772-500G; Milipore Sigma), and lysed 3 times in a MiniBeadBeater for 90 sec each at 4˚C. In between bead beating, samples were chilled in an ice bath for 2 min. Samples were then pelleted at 1000 g at 4˚C for 30 sec. Supernatants were transferred to a 1.5 mL microcentrifuge tube, and beads in screw-cap tubes were washed once again in the same lysis buffer plus protease inhibitors and pelleted like above. Supernatants of screw-cap tubes were transferred to same 1.5 mL tube as above, and were cleared of insoluble debris, twice at 16000 g for 10 min at 4˚C. A final clearance spin of lysates was done at 20000 g for 30 min at 4˚C. Protein concentrations were then quantified using the Pierce™ BCA Protein Assay Kit (Cat # 23227; Thermo Fisher Scientific) in a 96-well plate format (Cat # 353072; Corning). Sample absorbances were measured at 562 nm using a VersaMax Microplate Reader and SoftMax Pro Software. Absorbances were converted to protein concentration using a bovine serum albumin standard curve.

Immunoprecipitation (IP)

For immunoprecipitation, an mNeonGreen-Trap Agarose Kit (ntak-20; Chromotek) to pull down Bsc2-mNeonGreen (mNG) fusion protein was used, according to manufacturer's protocol. To begin, for each sample 25µL of agarose beads containing an anti-mNG nanobody were washed in 500µL of ice cold dilution buffer (10mM Tris-HCl pH 7.5, 150mM NaCl, 0.5mM EDTA, and 0.018% sodium azide), centrifuged down at 2500 g for 5 min at 4˚C, and buffer removed. 4000 µg of protein lysate from cold glass bead lysis for each sample was

centrifuged at 16000 g, 5 min, at 4˚C. Then, lysates were incubated with the washed mNG beads and rotated end over end for 1 hr at 4˚C. Samples were then spun down at 2500 g for 5 min at 4˚C and supernatants removed. Beads were then washed three times in 500µL wash buffer (10 mM Tris/Cl pH 7.5, 150 mM NaCl, 0.05 % Nonidet™ P40 Substitute, 0.5 mM EDTA, and 0.018 % sodium azide) and centrifuged like above, in between each wash. After final wash and spin, supernatant was removed, beads were transferred to a fresh 1.5 mL tube. 2X Laemmli sample buffer was added to beads, and samples were boiled for 5 min at 95˚C

LC-MS/MS proteomics

Following boiling step, IP samples were centrifuged at 2500 g, for 2 min at 4˚C to pellet beads. The entirety of each supernatant was loaded onto a 10% mini-protean TGX gel (4561033; Bio-Rad). Samples were subjected to electrophoresis at 90 V constant until the dye front was ∼10 cm into the gel. The gel was subsequently removed from the casing and stained with Coomassie reagent (0.5 Coomassie G-250, 50% methanol, 10%

acetic acid) for 10 min on an RT rocker. The gel was then rinsed three times in sterile Mili-Q water to gently destain. Once the gel was sufficiently destained, 10-cm gel bands were excised from each lane, taking care to exclude the stacking gel and dye front. Gel bands were further cut into 1-mm squares and placed into sterile microcentrifuge tubes. Samples were digested overnight with trypsin (Pierce) following reduction and alkylation with DTT and iodoacetamide (Sigma-Aldrich). The samples then underwent solid-phase extraction cleanup with an Oasis HLB plate (Waters), and the resulting samples were injected onto an Orbitrap Fusion Lumos mass spectrometer coupled to an Ultimate 3000 RSLC-Nano liquid

chromatography system. Samples were injected onto a 75 μm i.d., 75-cm long EasySpray column (Thermo Fisher Scientific) and eluted with a gradient from 0 to 28% buffer B over 90 min. The buffer contained 2% (vol/vol) acetonitrile and 0.1% formic acid in water, and buffer B contained 80% (vol/vol) acetonitrile, 10% (vol/vol) trifluoroethanol, and 0.1% formic acid in water. The mass spectrometer operated in positive ion mode with a source voltage of 1.5–2.0 kV and an ion transfer tube temperature of 275°C. MS scans were acquired at 120,000 resolution in the Orbitrap, and up to 10 MS/MS spectra were obtained in the ion trap for each full spectrum acquired using higher-energy collisional dissociation for ions with charges 2–7. Dynamic exclusion was set for 25 s after an ion was selected for fragmentation. RawMS data files were analyzed using Proteome Discoverer v 2.4 (Thermo Fisher Scientific), with peptide identification performed using Sequest HT searching against the *Saccharomyces cerevisiae* protein database from UniProt. Fragment and precursor tolerances of 10 ppm and 0.6 dalton were specified, and three missed cleavages were allowed. Carbamidomethylation of Cys was set as a fixed modification, with oxidation of Met set as a variable modification. The false-discovery rate cutoff was 1% for all peptides.

Cell culture

U2-OS cells were cultured in DMEM (D5796; Sigma) supplemented with 10% Cosmic Calf Serum (SH30087.04; Hyclone), 1% penicillin streptomycin solution (30-002-Cl; Corning), and 25mM HEPES (H0887;Sigma). The cells were passaged when they reached 80–90% confluence with 0.25% trypsin-EDTA (25-053-Cl; Corning). To promote LD biogenesis, cells

were incubated with 600 μM of OA conjugated with 100 μM of FA-free BSA (A8806; Sigma-Aldrich) for 16 hours.

Cloning and transient transfection

Full length Bsc2-EGFP was generated after PCR amplification of full length Bsc2 from a yeast pBP73G Bsc2 untagged overexpression plasmid and cloning into pEGFP-N2 (XhoI/BamHI). pEGFP-N2 alone, served as a negative control. The plasmids were transfected into U2-OS cells using Lipofectamine 3000 Transfection Reagent (L3000001; Invitrogen) and Opti-MEM (31985-070; Gibco) for 48 h before experiments.

IF staining

Cells were fixed with 4% PFA solution in PBS for 15 min at RT. For IF staining, fixed cells were washed with PBS, permeabilized with 0.2% NP-40 in PBS at RT for 3 min, and blocked in IF buffer (PBS containing 3% BSA, 0.1% NP-40, and 0.02% sodium azide) for 45 min. The cells were then incubated with primary antibody in IF buffer for 1 h, washed thrice with PBS, incubated with secondary antibody in IF buffer for 30 min, and given two washes with PBS. Cells were then incubated with MDH AutoDOT (SM1000a; 1:1,000 dilution; Abcepta) for 15 min, washed thrice with PBS, and then stored in PBS at 4˚C before imaging. The primary antibody used was mouse anti-Hsp90B1 (AMAb91019; 1:100 dilution; Sigma-Aldrich). The secondary antibody used was donkey anti-mouse Rhodamine Red-X (715-295-151; 1:1,000 dilution; Jackson Laboratories). LDs were visualized by staining the cells with AutoDOT.

Fluorescence microscopy

For confocal microscopy, yeast cells were grown as described above and collected by centrifugation at 4,000 rpm for 5 min. Where indicated, cells were incubated for 5 min with MDH (SM1000a; Abcepta) at a final concentration of 0.1 mM to visualize LDs.

Before imaging, yeast cells were washed with 1 ml of Mili-Q water and resuspended in 50-100µL of Mili-Q water. Mammalian cells were imaged in 8-well Nunc™ Lab-Tek™ II chambered coverglass (Cat #154409; Thermo Scientific). All images were taken as single slices at approximately mid-plane using a Zeiss LSM880 inverted laser scanning confocal microscope equipped with Zen software. Images were taken with a 63x oil objective NA = 1.4 or 40x oil objective NA = 1.4 at RT, unless noted otherwise. Approximately seven Z-sections of each image were taken for yeast, and four for mammalian cells. The merged images were maximum intensity z-projections, generated by Fiji. For epifluorescence microscopy, cells were grown, stained, and collected as described above. Imaging was performed on an EVOS FL Cell Imaging System at RT.

Yeast strain generation and plasmid construction

A modified version of the lithium acetate method was used for the generation of all yeast knock outs and knock ins. Briefly, yeast were diluted from a ~24h culture to an OD_{600} = 0.001 in YPD media and allowed to grow 16-20h, overnight, until they reached OD600 = 0.6. For each transformation, the entire culture was pelleted (50mL), washed with sterile Mili-Q water, washed with 0.1 M lithium acetate, pelleted and resuspended in 1mL 0.1M lithium acetate. 100µL this yeast-lithium acetate suspension was added to ~1mL of transformation solution

(40% polyethylene glycol in 0.1 M lithium acetate, 0.25 µg/µl single-stranded carrier DNA [D9156; Sigma-Aldrich]) supplemented with 5-10µg of PCR product. Transformations were vortexed and incubated at 30˚C for 45 min, then 42˚C for 30 min. Cells were then pelleted at 2000 g, 2 min and gently washed with sterile Mili-Q water, then pelleted again. For antibiotic marker transformations, yeast were then resuspended in 2mL fresh YPD media and allowed to recover overnight, 30˚C, 225 RPM. The following day, cells were pelleted and plated onto YPD plates containing antibiotic and incubated at 30˚C, 2-3 d. For auxotrophic marker transformations, yeast were plated onto SC dropout plates same day (immediately after Mili-Q washing step) and incubated at 30˚C, 2-3 d. Plasmids were generated for this study using Gibson Assembly following the manufacturer's protocol (E2611; NEB). All pBP73-G vectors were cut with XbaI and XhoI. For yeast plasmid transformations, cells were grown in YPD media, overnight until saturation. 1 mL of overnight culture was pelleted at 12000 RPM, 2 min at RT. Pellets were then washed in 0.1M Lithium Acetate and centrifuged again, like above. Yeast cells were then resuspended in ~300 µL transformation solution (40% polyethylene glycol in 0.1 M lithium acetate, 0.25 µg/µl single-stranded carrier DNA [D9156; Sigma-Aldrich]) with 1µg of plasmid DNA, vortexed briefly, and incubated at RT for 1hr. Transformations were then gently mixed, DMSO added to a final concentration of 10%, and heat shocked at 42˚C, 10 min. Samples were then put on ice for 2 min, then entire reaction was plated onto SCD plates lacking uracil, and incubated at 30˚C for 2-3 days.

Proteomics quantification

Proteomics quantification and analysis were performed using Excel. All samples were analyzed in triplicate. To adjust for total protein differences between samples, the sum of all spectral counts within each sample was taken and divided by the average of the spectral count sums in the empty vector soluble mNG (EV-mNG) samples. This ensured differences observed in the proteomics data are not due to unequal "loading" into the MS. Next, only proteins with detectable spectral counts in all 3 replicates of the Bsc2-mNG IP samples were considered for analyses, regardless of whether they were present in the EV-mNG IP replicates. From this list proteins, those with undetectable spectral counts in the EV-mNG IP replicates had their spectral counts changed from "0" to "1" to aid in quantifications for statistical analysis. To generate a high-confidence list of Bsc2 interacting proteins, the average spectral counts of each protein from the Bsc2-mNG IPs were divided by the corresponding average spectral counts from the EV-mNG IP samples. Therefore, proteins more abundant in the Bsc2-mNG IP samples would produce a ratio >0. To generate volcano plots in GraphPad Prism, $\log_2$ values were calculated for the ratio of average protein expression in EV-mNG and Bsc2-mNG (i.e., $\log_2$[protein A in Bsc2-mNG/protein A in EV-mNG]). Then, the p-value for significance of the abundance for each protein in EV-mNG and Bsc2-mNG replicate samples was calculated via t test. Finally, the $-\log_{10}$ of these p-values was calculated and plotted against the above log2 values in volcano plot form. Significance cut-off on the y-axis was the -log10 of P = 0.05, or 1.3.

Cartoon development

All cartoons created with BioRender.com or Microsoft Powerpoint. For Figure 2.2A, the hydrophobicity plot was generated using data collected from Phobius open access hydrophobicity predictor (Käll et al., 2004) and the helical wheel generated using HeliQuest (Gautier et al., 2008).

CHAPTER FOUR

Discussion and Future Directions

Significance

Emerging data indicates that, on the cellular level, there are distinct LD subpopulations that highly differ in their composition and function. However, how LD heterogeneity arises and how it influences LD function and cellular physiology remain glaring, open questions. **The goal of my research was to use Bsc2 as a model protein to study and more clearly understand the interplay between the protein identity of a LD subpopulation and its ultimate role within the cell.** Although, at the moment, there is no known mammalian ortholog of Bsc2, the putative Class I and II mechanisms through which proteins interact with LD monolayers is conserved to an extent, making budding yeast an ideal platform to study why specific proteins associate with LD subsets and how they alter metabolic homeostasis. In chapter two of this dissertation, I have demonstrated that Bsc2 targets to a specific subpopulation of LDs that are enriched in TG, where it negatively regulates TG lipolysis. Imaging and fragment analyses determined that Bsc2 requires both HR1 and HR2 regions to stably associate with LDs, while full length Bsc2 targets to LDs outside of yeast in U2OS cells fed with OA, further indicating a preference for TG-enriched LDs. In line with yeast fragment analyses, MD simulations of Bsc2 hydrophobic regions reveal key conformational changes when Bsc2 is targeted to TG-rich LD monolayer, its preferred environment, where polar residues anchor and stabilize this interaction. Conversely, modeling Bsc2 interactions with a SE-enriched LD monolayer or an ER bilayer disrupt the necessary conformations of the Bsc2

hydrophobic regions needed for stable LD association, results which mirrored imaging in which Bsc2 appears to lose stability and targeting in yeast genetically manipulated to contain SE only LDs. Although not direct evidence, these simulations are highly supportive of Bsc2 specificity for TG-containing LDs. These findings are quite exciting as they shed some light on how the NL composition of the LD affects the protein composition of the LD, which is largely unknown.

Functionally, deletion and overexpression data outlined in chapter two establish Bsc2 as a negative regulator of TG lipolysis. Loss of Bsc2 enhances TG lipolysis in a manner that is dependent on the major TG lipase, Tgl3, and as Bsc2 mutants enter late stationary phase, they experience a shortage of LDs. Conversely, Bsc2 overexpressing yeast accumulate striking amounts of whole-cell TG, as well as jumbo-sized LDs. Interestingly, my work shows that Bsc2 does not stably interact with Tgl3 or alter the ability of it, or the other TG lipases, to target LDs. The mechanism by which Bsc2 influences Tgl3-dependent TG lipolysis remains elusive, but the imaging, biochemistry, and modeling data suggest that Bsc2 may compete with Tgl3 for TG binding and this model will is the subject of further studies.

Collectively, the major findings of my dissertation reveal that Bsc2 is a novel regulator of TG lipolysis, that localizes to a subset of LDs due to its preference for TG-rich LDs. These findings advance the field of LD biology on several levels, but in particular, provide an understanding of the factors that govern LD protein identity and functional diversity, as well as define a putative mechanism for the regulation of TG lipolysis in yeast.

Future Directions

Although the work outlined in chapter two of this thesis has begun to characterize the role of LD subpopulation marker Bsc2, there are a number of future studies to be performed in regards to determining how the specificity of Bsc2 for TG, arises. As demonstrated by MD simulations and fluorescence imaging, Bsc2 appears to specifically target and interact with TG-containing LDs, but it is pertinent to confirm these findings, biochemically. It has been previously shown that major TG lipase Tgl3 prefers to hydrolyze TG containing C14:0, C16:0, and C26:0 (Athenstaedt and Daum, 2005; Kurat et al., 2006). Therefore, it is highly possible for the protected Bsc2-positive LD subpopulation to be enriched TG containing these long chain fatty acids. Key insights can be gained by employing lipidomics profiling of Bsc2-positive versus Bsc2-negative LDs and determining the true composition of the NL core for this subset of LDs. In line with this, mammalian cells have provided a powerful tool in dissecting the functional heterogeneity of LDs. As such, our U2OS mammalian system allows for seamless manipulation of the NL core contents in LDs, simply by feeding cells with OA to produce TG-rich LDs or feeding with cyclodextrin to produce SE-rich LDs. These treatments are ideal for assessing the ability of Bsc2 to target to different NL-containing LDs as they do not require genetic manipulation of the NL synthesizing enzymes, like in yeast cells.

Secondary structure analysis paired with MD simulations of Bsc2-LD association determined that the HR2 region of Bsc2 contains 3 key polar resiudes Gln72, Cys75, and Ser76, located near the kink of the predicted hairpin are key for stabilizing Bsc2-TG interactions. Two outstanding questions in regards to *in vivo* function are: 1) Whether one or all of these residues are required for adequate protein-TG association? and 2) Are these residues important for

Bsc2's negative regulation of TG lipolysis? Therefore, imaging and functional analyses of Bsc2 HR2 point mutants will aid in addressing these questions.

Determining a specific mechanism for Bsc2-dependent inhibition of Tgl3 lipolytic activity has remained elusive, but is the prime focus of follow-up studies. **My current model for which there is the strongest evidence is that Bsc2 competes against Tgl3 for TG access via packing defects on a subpopulation of LDs.** Immunoprecipitation and mass spectrometry data shows that at steady state conditions, Bsc2 does not directly interact with Tgl3, yet there is still a possibility that this may be a weak, or transient interaction, dependent on metabolic cues, like cerulenin stimulated lipolysis. As such, it is important to test a putative physical interaction between Bsc2 and Tgl3 lipase, under the aforementioned conditions. Despite sequence and secondary structure analysis being unable to locate a direct Bsc2 ortholog in higher organisms, like mammals, this does not exclude the possibility that Bsc2 is a functional ortholog of peptide negative regulators of ATGL, like G0S2, which directly binds ATGL and inhibits lipolytic activity (Yang et al., 2010; Zhang et al., 2017). Given the high level of homology of the yeast TG lipases to the mammalian TG lipases, and the fact that much more is known regarding the regulatory mechanisms of ATGL lipolysis in mammals, this is a worthy avenue to pursue.

In closing . . .

Investigating of the functional heterogeneity of yeast LD subpopulations has proven to be exceptionally rewarding over the course of my graduate career. I can only hope that my work advances the field of LD biology's understanding of determintants of LD diversity and

protein targeting, but most importantly, generates greater appreciation for the use of budding yeast as a model system in metabolism research.

APPENDIX A

Table of Yeast Strains

Strain	Description	Parent	Mat
WT BY	his3Δ1 leu2Δ0 met15Δ0 ura3Δ0	BY4741	a
WT W303	leu2-3, 112 trp1-1 can1-100 ura3-1 ade2-1 his3-11,14	W303	a
Bsc2-GFP WT	Bsc2-GFP-G418 WT	BY4741	a
Bsc2-GFP Erg6-mRuby WT	Bsc2-GFP-G418 Erg6-mRuby3-NAT WT	BY4741	a
Bsc2-mNG WT	Bsc2-mNeonGreen::HYG WT	W303	a
Bsc2-mNG TG only	Bsc2-mNeonGreen-HYG are1Δ::HIS3 are2Δ::URA3	W303	a
Bsc2-mNG SE only	Bsc2-mNeonGreen-HYG dga1Δ::URA3 lro1Δ::LEU2	W303	a
$Bsc2^{FL}$	pBP73G GPDpr-$Bsc2^{FL}$-mNeonGreen-URA3 WT	BY4741	a
$Bsc2^{N\text{-}HR1+HR2}$	pBP73G GPDpr-$Bsc2^{N\text{-}HR1+HR2}$-mNeonGreen-URA3 WT	BY4741	a
$Bsc2^{HR1+HR2}$	pBP73G GPDpr-$Bsc2^{HR1+HR2}$-mNeonGreen-URA3 WT	BY4741	a
$Bsc2^{N\text{-}HR1}$	pBP73G GPDpr-$Bsc2^{N\text{-}HR1}$-mNeonGreen-URA3 WT	BY4741	a
$Bsc2^{HR1}$	pBP73G GPDpr-$Bsc2^{HR1}$-mNeonGreen-URA3 WT	BY4741	a
$Bsc2^{HR2}$	pBP73G GPDpr-$Bsc2^{HR2}$-mNeonGreen-URA3 WT	BY4741	a
$Bsc2^{LiveDrop}$	pBP73G GPDpr-$Bsc2^{FL(HR1::LiveDrop)}$-mNeonGreen-URA3 WT	BY4741	a
bsc2Δ	bsc2Δ::G418	BY4741	a
bsc2Δtgl3Δ	bsc2Δ::G418 tgl3Δ::HYG	BY4741	a
tgl3Δtgl4Δ tgl5Δ	tgl3Δ::G418 tgl4Δ::NAT tgl5Δ::HYG	BY4741	a
WT ^{GAL}DGA1	$^{GAL10::TRP1}$DGA1 lro1Δ are1Δ are2Δ	W303	a
bsc2Δ ^{GAL}DGA1	bsc2Δ::HYG $^{GAL10::TRP1}$DGA1 lro1Δ are1Δ are2Δ	W303	a
$Bsc2^{N\text{-}HR1+HR2}$-GFP	$Bsc2^{N\text{-}HR1+HR2}$-GFP-NAT	BY4741	a
EV-GFP WT	pBP73G GPDpr-Empty Vector-GFP-URA3 WT	BY4741	a
EV-mNG WT	pBP73G GPDpr-Empty Vector-mNeonGreen-URA3 WT	BY4741	a
Bsc2 OE WT	pBP73G GPDpr-Bsc2-mNeonGreen-URA3 WT	BY4741	a
Pln1 OE WT	pBP73G GPDpr-Pln1-mNeonGreen-URA3 WT	BY4741	a

Untagged Bsc2 OE WT	pBP73G GPDpr-Bsc2-URA3 WT	BY4741	a
Tgl3-GFP WT	Tgl3-GFP-HIS3 WT	BY4741	a
Tgl4-GFP WT	Tgl4-GFP-HIS3 WT	BY4741	a
Tgl5-GFP WT	Tgl5-GFP-HIS3 WT	BY4741	a
Tgl3-GFP bsc2Δ	Tgl3-GFP-HIS3 bsc2Δ::HYG	BY4741	a
Tgl4-GFP bsc2Δ	Tgl4-GFP-HIS3 bsc2Δ::HYG	BY4741	a
Tgl5-GFP bsc2Δ	Tgl5-GFP-HIS3 bsc2Δ::HYG	BY4741	a
Tgl3-GFP EV	Tgl3-GFP-HIS3 pRS316 Empty Vector-URA3 WT	BY4741	a
Tgl4-GFP EV	Tgl4-GFP-HIS3 pRS316 Empty Vector-URA3 WT	BY4741	a
Tgl5-GFP EV	Tgl5-GFP-HIS3 pRS316 Empty Vector-URA3 WT	BY4741	a
Tgl3-GFP Bsc2 OE	Tgl3-GFP-HIS3 pBP73G GPDpr-Bsc2-URA3	BY4741	a
Tgl4-GFP Bsc2 OE	Tgl4-GFP-HIS3 pBP73G GPDpr-Bsc2-URA3	BY4741	a
Tgl5-GFP Bsc2 OE	Tgl5-GFP-HIS3 pBP73G GPDpr-Bsc2-URA3	BY4741	a
Tgl3-GFP Bsc2 OE	Tgl3-GFP-HIS3 pBP73G GPDpr-Bsc2-URA3	BY4741	a
Bsc2-GFP Tgl3-mRuby WT	Bsc2-GFP-G418 Tgl3-mRuby3-NAT WT	BY4741	a

APPENDIX B

Table of Plasmids

Name	Description	Purpose	Source
EV-GFP	pBP73G GPDpr-Empty Vector-GFP-URA3	over-expression of soluble GFP from GPD promoter	This study
EV-mNG	pBP73G GPDpr-Empty Vector-mNeonGreen-URA3	over-expression of soluble mNG from GPD promoter	This study
EV untagged	pRS316 Empty Vector-URA3	over-expression of URA3 selection plasmid	This study
Bsc2 OE untagged	pBP73G GPDpr-Bsc2^{FL}-URA3	over-expression of full length untagged Bsc2 from GPD promoter	This study
Bsc2^{FL}/ Bsc2 OE	pBP73G GPDpr-Bsc2^{FL}-mNeonGreen-URA3	over-expression of full length Bsc2 from GPD promoter	This study
Bsc2$^{N\text{-}HR1+HR2}$	pBP73G GPDpr-Bsc2$^{N\text{-}HR1+HR2}$-mNeonGreen-URA3	over-expression of truncated Bsc2 from GPD promoter	This study
Bsc2$^{HR1+HR2}$	pBP73G GPDpr-Bsc2$^{HR1+HR2}$-mNeonGreen-URA3	over-expression of truncated Bsc2 from GPD promoter	This study
Bsc2$^{N\text{-}HR1}$	pBP73G GPDpr-Bsc2$^{N\text{-}HR1}$-mNeonGreen-URA3	over-expression of truncated Bsc2 from GPD promoter	This study
Bsc2^{HR1}	pBP73G GPDpr-Bsc2^{HR1}-mNeonGreen-URA3	over-expression of truncated Bsc2 from GPD promoter	This study
Bsc2^{HR2}	pBP73G GPDpr-Bsc2^{HR2}-mNeonGreen-URA3	over-expression of truncated Bsc2 from GPD promoter	This study
Bsc2^{LiveDrop}	pBP73G GPDpr-Bsc2$^{FL(HR1::LiveDrop)}$-mNeonGreen-URA3	over-expression of chimeric full length Bsc2 from GPD promoter	This study
Pln1 OE	pBP73G GPDpr-Pln1^{FL}-mNeonGreen-URA3	over-expression of full length Pln1 from GPD promoter	This study
EV-EGFP	pCMVpr-EGFP-N2	over-expression of soluble GFP for mammalian cells from CMV promoter	This study
Bsc2-EGFP	pCMVpr-Bsc2^{FL}-EGFP-N2	over-expression of full length Bsc2 for mammalian cells from CMV promoter	This study

BIBLIOGRAPHY

Abraham, M.J., T. Murtola, R. Schulz, S. Páll, J.C. Smith, B. Hess, and E. Lindahl. 2015. GROMACS: High performance molecular simulations through multi-level parallelism from laptops to supercomputers. *SoftwareX*. 1–2:19–25. doi:10.1016/j.softx.2015.06.001.

Arlt, H., X. Sui, B. Folger, C. Adams, X. Chen, R. Remme, F.A. Hamprecht, F. DiMaio, M. Liao, J.M. Goodman, R.V. Farese, and T.C. Walther. 2022. Seipin forms a flexible cage at lipid droplet formation sites. *Nat. Struct. Mol. Biol.* 29:194–202. doi:10.1038/s41594-021-00718-y.

Athenstaedt, K., and G. Daum. 2003. YMR313c/TGL3 Encodes a Novel Triacylglycerol Lipase Located in Lipid Particles of Saccharomyces cerevisiae. *J. Biol. Chem.* 278:23317–23323. doi:10.1074/jbc.M302577200.

Athenstaedt, K., and G. Daum. 2005. Tgl4p and Tgl5p, Two Triacylglycerol Lipases of the Yeast Saccharomyces cerevisiae Are Localized to Lipid Particles. *J. Biol. Chem.* 280:37301–37309. doi:10.1074/jbc.M507261200.

Athenstaedt, K., D. Zweytick, A. Jandrositz, S.D. Kohlwein, and G. Daum. 1999. Identification and Characterization of Major Lipid Particle Proteins of the Yeast *Saccharomyces cerevisiae*. *J. Bacteriol.* 181:6441–6448. doi:10.1128/JB.181.20.6441-6448.1999.

Azzaz, F., N. Yahi, H. Chahinian, and J. Fantini. 2022. The Epigenetic Dimension of Protein Structure Is an Intrinsic Weakness of the AlphaFold Program. *Biomolecules*. 12:1527. doi:10.3390/biom12101527.

Bacle, A., R. Gautier, C.L. Jackson, P.F.J. Fuchs, and S. Vanni. 2017. Interdigitation between Triglycerides and Lipids Modulates Surface Properties of Lipid Droplets. *Biophys. J.* 112:1417–1430. doi:10.1016/j.bpj.2017.02.032.

Baek, M., F. DiMaio, I. Anishchenko, J. Dauparas, S. Ovchinnikov, G.R. Lee, J. Wang, Q. Cong, L.N. Kinch, R.D. Schaeffer, C. Millán, H. Park, C. Adams, C.R. Glassman, A. DeGiovanni, J.H. Pereira, A.V. Rodrigues, A.A. van Dijk, A.C. Ebrecht, D.J. Opperman, T. Sagmeister, C. Buhlheller, T. Pavkov-Keller, M.K. Rathinaswamy, U. Dalwadi, C.K. Yip, J.E. Burke, K.C. Garcia, N.V. Grishin, P.D. Adams, R.J. Read, and D. Baker. 2021. Accurate prediction of protein structures and interactions using a three-track neural network. *Science*. 373:871–876. doi:10.1126/science.abj8754.

Barducci, A., G. Bussi, and M. Parrinello. 2008. Well-Tempered Metadynamics: A Smoothly Converging and Tunable Free-Energy Method. *Phys. Rev. Lett.* 100:020603. doi:10.1103/PhysRevLett.100.020603.

Becuwe, M., L.M. Bond, A.F.M. Pinto, S. Boland, N. Mejhert, S.D. Elliott, M. Cicconet, M.M. Graham, X.N. Liu, O. Ilkayeva, A. Saghatelian, T.C. Walther, and R.V. Farese. 2020. FIT2 is an acyl–coenzyme A diphosphatase crucial for endoplasmic reticulum homeostasis. *J. Cell Biol.* 219:e202006111. doi:10.1083/jcb.202006111.

Ben M'barek, K., D. Ajjaji, A. Chorlay, S. Vanni, L. Forêt, and A.R. Thiam. 2017. ER Membrane Phospholipids and Surface Tension Control Cellular Lipid Droplet Formation. *Dev. Cell.* 41:591-604.e7. doi:10.1016/j.devcel.2017.05.012.

Bersuker, K., C.W.H. Peterson, M. To, S.J. Sahl, V. Savikhin, E.A. Grossman, D.K. Nomura, and J.A. Olzmann. 2018. A Proximity Labeling Strategy Provides Insights into the Composition and Dynamics of Lipid Droplet Proteomes. *Dev. Cell.* 44:97-112.e7. doi:10.1016/j.devcel.2017.11.020.

Binns, D., T. Januszewski, Y. Chen, J. Hill, V.S. Markin, Y. Zhao, C. Gilpin, K.D. Chapman, R.G.W. Anderson, and J.M. Goodman. 2006. An intimate collaboration between peroxisomes and lipid bodies. *J. Cell Biol.* 173:719–731. doi:10.1083/jcb.200511125.

Binns, D., S. Lee, C.L. Hilton, Q.-X. Jiang, and J.M. Goodman. 2010. Seipin Is a Discrete Homooligomer. *Biochemistry*. 49:10747–10755. doi:10.1021/bi1013003.

Braun, R.J., and J.M.J. Swanson. 2022. Capturing the Liquid-Crystalline Phase Transformation: Implications for Protein Targeting to Sterol Ester-Rich Lipid Droplets. *Membranes*. 12:949. doi:10.3390/membranes12100949.

Caillon, L., V. Nieto, P. Gehan, M. Omrane, N. Rodriguez, L. Monticelli, and A.R. Thiam. 2020. Triacylglycerols sequester monotopic membrane proteins to lipid droplets. *Nat. Commun.* 11:3944. doi:10.1038/s41467-020-17585-8.

Campomanes, P., J. Prabhu, V. Zoni, and S. Vanni. 2021. Recharging your fats: CHARMM36 parameters for neutral lipids triacylglycerol and diacylglycerol. *Biophys. Rep.* 1:None. doi:10.1016/j.bpr.2021.100034.

Cartwright, B.R., D.D. Binns, C.L. Hilton, S. Han, Q. Gao, and J.M. Goodman. 2015. Seipin performs dissectible functions in promoting lipid droplet biogenesis and regulating droplet morphology. *Mol. Biol. Cell*. 26:726–739. doi:10.1091/mbc.E14-08-1303.

Chorlay, A., L. Forêt, and A.R. Thiam. 2021. Origin of gradients in lipid density and surface tension between connected lipid droplet and bilayer. *Biophys. J.* 120:5491–5503. doi:10.1016/j.bpj.2021.11.022.

Chorlay, A., and A.R. Thiam. 2020. Neutral lipids regulate amphipathic helix affinity for model lipid droplets. *J. Cell Biol.* 219:e201907099. doi:10.1083/jcb.201907099.

Choudhary, V., N. Ojha, A. Golden, and W.A. Prinz. 2015. A conserved family of proteins facilitates nascent lipid droplet budding from the ER. *J. Cell Biol.* 211:261–271. doi:10.1083/jcb.201505067.

Čopič, A., S. Antoine-Bally, M. Giménez-Andrés, C. La Torre Garay, B. Antonny, M.M. Manni, S. Pagnotta, J. Guihot, and C.L. Jackson. 2018. A giant amphipathic helix from a perilipin that is adapted for coating lipid droplets. *Nat. Commun.* 9:1332. doi:10.1038/s41467-018-03717-8.

Currie, E., X. Guo, R. Christiano, C. Chitraju, N. Kory, K. Harrison, J. Haas, T.C. Walther, and R.V. Farese. 2014. High confidence proteomic analysis of yeast LDs identifies additional droplet proteins and reveals connections to dolichol synthesis and sterol acetylation. *J. Lipid Res.* 55:1465–1477. doi:10.1194/jlr.M050229.

DeCaprio, J., and T.O. Kohl. 2020. Lysing Yeast Cells with Glass Beads for Immunoprecipitation. *Cold Spring Harb. Protoc.* 2020:pdb.prot098590. doi:10.1101/pdb.prot098590.

Dhiman, R., S. Caesar, A.R. Thiam, and B. Schrul. 2020. Mechanisms of protein targeting to lipid droplets: A unified cell biological and biophysical perspective. *Semin. Cell Dev. Biol.* 108:4–13. doi:10.1016/j.semcdb.2020.03.004.

Dobson, L., L.I. Szekeres, C. Gerdán, T. Langó, A. Zeke, and G.E. Tusnády. 2023. TmAlphaFold database: membrane localization and evaluation of AlphaFold2 predicted alpha-helical transmembrane protein structures. *Nucleic Acids Res.* 51:D517–D522. doi:10.1093/nar/gkac928.

Duelund, L., G.V. Jensen, H.K. Hannibal-Bach, C.S. Ejsing, J.S. Pedersen, K.I. Pakkanen, and J.H. Ipsen. 2013. Composition, structure and properties of POPC–triolein mixtures. Evidence of triglyceride domains in phospholipid bilayers. *Biochim. Biophys. Acta BBA - Biomembr.* 1828:1909–1917. doi:10.1016/j.bbamem.2013.03.020.

Duncan, R.E., M. Ahmadian, K. Jaworski, E. Sarkadi-Nagy, and H.S. Sul. 2007. Regulation of Lipolysis in Adipocytes. *Annu. Rev. Nutr.* 27:79–101. doi:10.1146/annurev.nutr.27.061406.093734.

Eisenberg-Bord, M., M. Mari, U. Weill, E. Rosenfeld-Gur, O. Moldavski, I.G. Castro, K.G. Soni, N. Harpaz, T.P. Levine, A.H. Futerman, F. Reggiori, V.A. Bankaitis, M. Schuldiner, and M. Bohnert. 2018. Identification of seipin-linked factors that act as determinants of a lipid droplet subpopulation. *J. Cell Biol.* 217:269–282. doi:10.1083/jcb.201704122.

Essmann, U., L. Perera, M.L. Berkowitz, T. Darden, H. Lee, and L.G. Pedersen. 1995. A smooth particle mesh Ewald method. *J. Chem. Phys.* 103:8577–8593. doi:10.1063/1.470117.

Fei, W., G. Shui, B. Gaeta, X. Du, L. Kuerschner, P. Li, A.J. Brown, M.R. Wenk, R.G. Parton, and H. Yang. 2008. Fld1p, a functional homologue of human seipin, regulates the size of lipid droplets in yeast. *J. Cell Biol.* 180:473–482. doi:10.1083/jcb.200711136.

Fei, W., G. Shui, Y. Zhang, N. Krahmer, C. Ferguson, T.S. Kapterian, R.C. Lin, I.W. Dawes, A.J. Brown, P. Li, X. Huang, R.G. Parton, M.R. Wenk, T.C. Walther, and H. Yang. 2011. A Role for Phosphatidic Acid in the Formation of "Supersized" Lipid Droplets. *PLoS Genet.* 7:e1002201. doi:10.1371/journal.pgen.1002201.

Gao, Q., D.D. Binns, L.N. Kinch, N.V. Grishin, N. Ortiz, X. Chen, and J.M. Goodman. 2017. Pet10p is a yeast perilipin that stabilizes lipid droplets and promotes their assembly. *J. Cell Biol.* 216:3199–3217. doi:10.1083/jcb.201610013.

Gaspar, M.L., H.F. Hofbauer, S.D. Kohlwein, and S.A. Henry. 2011. Coordination of Storage Lipid Synthesis and Membrane Biogenesis. *J. Biol. Chem.* 286:1696–1708. doi:10.1074/jbc.M110.172296.

Gautier, R., D. Douguet, B. Antonny, and G. Drin. 2008. HELIQUEST: a web server to screen sequences with specific α-helical properties. *Bioinformatics*. 24:2101–2102. doi:10.1093/bioinformatics/btn392.

Giménez-Andrés, M., A. Čopič, and B. Antonny. 2018. The Many Faces of Amphipathic Helices. *Biomolecules*. 8:45. doi:10.3390/biom8030045.

Gluchowski, N.L., M. Becuwe, T.C. Walther, and R.V. Farese. 2017. Lipid droplets and liver disease: from basic biology to clinical implications. *Nat. Rev. Gastroenterol. Hepatol.* 14:343–355. doi:10.1038/nrgastro.2017.32.

Gowers, R., M. Linke, J. Barnoud, T. Reddy, M. Melo, S. Seyler, J. Domański, D. Dotson, S. Buchoux, I. Kenney, and O. Beckstein. 2016. MDAnalysis: A Python Package for the Rapid Analysis of Molecular Dynamics Simulations. Austin, Texas. 98–105.

Grillitsch, K., M. Connerth, H. Köfeler, T.N. Arrey, B. Rietschel, B. Wagner, M. Karas, and G. Daum. 2011. Lipid particles/droplets of the yeast Saccharomyces cerevisiae revisited: Lipidome meets Proteome. *Biochim. Biophys. Acta BBA - Mol. Cell Biol. Lipids*. 1811:1165–1176. doi:10.1016/j.bbalip.2011.07.015.

Grippa, A., L. Buxó, G. Mora, C. Funaya, F.-Z. Idrissi, F. Mancuso, R. Gomez, J. Muntanyà, E. Sabidó, and P. Carvalho. 2015. The seipin complex Fld1/Ldb16 stabilizes ER–lipid droplet contact sites. *J. Cell Biol.* 211:829–844. doi:10.1083/jcb.201502070.

Han, S., D.D. Binns, Y.-F. Chang, and J.M. Goodman. 2015. Dissecting seipin function: the localized accumulation of phosphatidic acid at ER/LD junctions in the absence of seipin is suppressed by Sei1pΔNterm only in combination with Ldb16p. *BMC Cell Biol.* 16:29. doi:10.1186/s12860-015-0075-3.

Hariri, H., S. Rogers, R. Ugrankar, Y.L. Liu, J.R. Feathers, and W.M. Henne. 2018. Lipid droplet biogenesis is spatially coordinated at ER –vacuole contacts under nutritional stress. *EMBO Rep.* 19:57–72. doi:10.15252/embr.201744815.

Hariri, H., N. Speer, J. Bowerman, S. Rogers, G. Fu, E. Reetz, S. Datta, J.R. Feathers, R. Ugrankar, D. Nicastro, and W.M. Henne. 2019. Mdm1 maintains endoplasmic reticulum homeostasis by spatially regulating lipid droplet biogenesis. *J. Cell Biol.* 218:1319–1334. doi:10.1083/jcb.201808119.

Hegedűs, T., M. Geisler, G.L. Lukács, and B. Farkas. 2022. Ins and outs of AlphaFold2 transmembrane protein structure predictions. *Cell. Mol. Life Sci.* 79:73. doi:10.1007/s00018-021-04112-1.

Heier, C., and R.P. Kühnlein. 2018. Triacylglycerol Metabolism in *Drosophila melanogaster*. *Genetics*. 210:1163–1184. doi:10.1534/genetics.118.301583.

Heier, C., U. Taschler, S. Rengachari, M. Oberer, H. Wolinski, K. Natter, S.D. Kohlwein, R. Leber, and R. Zimmermann. 2010. Identification of Yju3p as functional orthologue of mammalian monoglyceride lipase in the yeast Saccharomyces cerevisiae. *Biochim. Biophys. Acta BBA - Mol. Cell Biol. Lipids*. 1801:1063–1071. doi:10.1016/j.bbalip.2010.06.001.

Hess, B. 2008. P-LINCS: A Parallel Linear Constraint Solver for Molecular Simulation. *J. Chem. Theory Comput.* 4:116–122. doi:10.1021/ct700200b.

Hinson, E.R., and P. Cresswell. 2009. The antiviral protein, viperin, localizes to lipid droplets via its N-terminal amphipathic α-helix. *Proc. Natl. Acad. Sci.* 106:20452–20457. doi:10.1073/pnas.0911679106.

Hoover, W.G. 1985. Canonical dynamics: Equilibrium phase-space distributions. *Phys. Rev. A.* 31:1695–1697. doi:10.1103/PhysRevA.31.1695.

Humphrey, W., A. Dalke, and K. Schulten. 1996. VMD: visual molecular dynamics. *J. Mol. Graph.* 14:33–38, 27–28. doi:10.1016/0263-7855(96)00018-5.

Jacquier, N., V. Choudhary, M. Mari, A. Toulmay, F. Reggiori, and R. Schneiter. 2011. Lipid droplets are functionally connected to the endoplasmic reticulum in *Saccharomyces cerevisiae*. *J. Cell Sci.* 124:2424–2437. doi:10.1242/jcs.076836.

Jo, S., T. Kim, V.G. Iyer, and W. Im. 2008. CHARMM-GUI: A web-based graphical user interface for CHARMM. *J. Comput. Chem.* 29:1859–1865. doi:10.1002/jcc.20945.

Jumper, J., R. Evans, A. Pritzel, T. Green, M. Figurnov, O. Ronneberger, K. Tunyasuvunakool, R. Bates, A. Žídek, A. Potapenko, A. Bridgland, C. Meyer, S.A.A. Kohl, A.J. Ballard, A. Cowie, B. Romera-Paredes, S. Nikolov, R. Jain, J. Adler, T. Back, S. Petersen, D. Reiman, E. Clancy, M. Zielinski, M. Steinegger, M. Pacholska, T. Berghammer, S. Bodenstein, D. Silver, O. Vinyals, A.W. Senior, K. Kavukcuoglu, P. Kohli, and D. Hassabis. 2021. Highly accurate protein structure prediction with AlphaFold. *Nature*. 596:583–589. doi:10.1038/s41586-021-03819-2.

Kadereit, B., P. Kumar, W.-J. Wang, D. Miranda, E.L. Snapp, N. Severina, I. Torregroza, T. Evans, and D.L. Silver. 2008. Evolutionarily conserved gene family important for fat storage. *Proc. Natl. Acad. Sci.* 105:94–99. doi:10.1073/pnas.0708579105.

Käll, L., A. Krogh, and E.L.L. Sonnhammer. 2004. A Combined Transmembrane Topology and Signal Peptide Prediction Method. *J. Mol. Biol.* 338:1027–1036. doi:10.1016/j.jmb.2004.03.016.

Khandelia, H., L. Duelund, K.I. Pakkanen, and J.H. Ipsen. 2010. Triglyceride Blisters in Lipid Bilayers: Implications for Lipid Droplet Biogenesis and the Mobile Lipid Signal in Cancer Cell Membranes. *PLoS ONE*. 5:e12811. doi:10.1371/journal.pone.0012811.

Kim, S., M.I. Oh, and J.M.J. Swanson. 2021. Stressed Lipid Droplets: How Neutral Lipids Relieve Surface Tension and Membrane Expansion Drives Protein Association. *J. Phys. Chem. B.* 125:5572–5586. doi:10.1021/acs.jpcb.1c01795.

Klauda, J.B., R.M. Venable, J.A. Freites, J.W. O'Connor, D.J. Tobias, C. Mondragon-Ramirez, I. Vorobyov, A.D. MacKerell, and R.W. Pastor. 2010. Update of the CHARMM All-Atom Additive Force Field for Lipids: Validation on Six Lipid Types. *J. Phys. Chem. B.* 114:7830–7843. doi:10.1021/jp101759q.

Klein, I., L. Klug, C. Schmidt, M. Zandl, M. Korber, G. Daum, and K. Athenstaedt. 2016. Regulation of the yeast triacylglycerol lipases Tgl4p and Tgl5p by the presence/absence of nonpolar lipids. *Mol. Biol. Cell*. 27:2014–2024. doi:10.1091/mbc.E15-09-0633.

Klug, Y.A., J.C. Deme, R.A. Corey, M.F. Renne, P.J. Stansfeld, S.M. Lea, and P. Carvalho. 2021. Mechanism of lipid droplet formation by the yeast Sei1/Ldb16 Seipin complex. *Nat. Commun.* 12:5892. doi:10.1038/s41467-021-26162-6.

Koch, B., C. Schmidt, B. Ploier, and G. Daum. 2014. Modifications of the C terminus Affect Functionality and Stability of Yeast Triacylglycerol Lipase Tgl3p. *J. Biol. Chem.* 289:19306–19316. doi:10.1074/jbc.M114.556944.

Koliwad, S.K., R.S. Streeper, M. Monetti, I. Cornelissen, L. Chan, K. Terayama, S. Naylor, M. Rao, B. Hubbard, and R.V. Farese. 2010. DGAT1-dependent triacylglycerol storage by macrophages protects mice from diet-induced insulin resistance and inflammation. *J. Clin. Invest.* 120:756–767. doi:10.1172/JCI36066.

Kory, N., R.V. Farese, and T.C. Walther. 2016. Targeting Fat: Mechanisms of Protein Localization to Lipid Droplets. *Trends Cell Biol.* 26:535–546. doi:10.1016/j.tcb.2016.02.007.

Kory, N., A.-R. Thiam, R.V. Farese, and T.C. Walther. 2015. Protein Crowding Is a Determinant of Lipid Droplet Protein Composition. *Dev. Cell*. 34:351–363. doi:10.1016/j.devcel.2015.06.007.

Kurat, C.F., K. Natter, J. Petschnigg, H. Wolinski, K. Scheuringer, H. Scholz, R. Zimmermann, R. Leber, R. Zechner, and S.D. Kohlwein. 2006. Obese Yeast: Triglyceride Lipolysis Is Functionally Conserved from Mammals to Yeast. *J. Biol. Chem.* 281:491–500. doi:10.1074/jbc.M508414200.

Laemmli, U.K. 1970. Cleavage of Structural Proteins during the Assembly of the Head of Bacteriophage T4. *Nature*. 227:680–685. doi:10.1038/227680a0.

Lass, A., R. Zimmermann, G. Haemmerle, M. Riederer, G. Schoiswohl, M. Schweiger, P. Kienesberger, J.G. Strauss, G. Gorkiewicz, and R. Zechner. 2006. Adipose triglyceride lipase-mediated lipolysis of cellular fat stores is activated by CGI-58 and defective in Chanarin-Dorfman Syndrome. *Cell Metab.* 3:309–319. doi:10.1016/j.cmet.2006.03.005.

Li, Z., K. Thiel, P.J. Thul, M. Beller, R.P. Kühnlein, and M.A. Welte. 2012. Lipid Droplets Control the Maternal Histone Supply of Drosophila Embryos. *Curr. Biol.* 22:2104–2113. doi:10.1016/j.cub.2012.09.018.

Listenberger, L.L., X. Han, S.E. Lewis, S. Cases, R.V. Farese, D.S. Ory, and J.E. Schaffer. 2003. Triglyceride accumulation protects against fatty acid-induced lipotoxicity. *Proc. Natl. Acad. Sci.* 100:3077–3082. doi:10.1073/pnas.0630588100.

Magré, J., M. Delépine, E. Khallouf, T. Gedde-Dahl, L. Van Maldergem, E. Sobel, J. Papp, M. Meier, A. Mégarbané, BSCL Working Group, M. Lathrop, and J. Capeau. 2001. Identification of the gene altered in Berardinelli–Seip congenital lipodystrophy on chromosome 11q13. *Nat. Genet.* 28:365–370. doi:10.1038/ng585.

Müllner, H., D. Zweytick, R. Leber, F. Turnowsky, and G. Daum. 2004. Targeting of proteins involved in sterol biosynthesis to lipid particles of the yeast Saccharomyces cerevisiae. *Biochim. Biophys. Acta BBA - Biomembr.* 1663:9–13. doi:10.1016/j.bbamem.2004.03.001.

Nosé, S. 1984. A unified formulation of the constant temperature molecular dynamics methods. *J. Chem. Phys.* 81:511–519. doi:10.1063/1.447334.

Olarte, M.-J., S. Kim, M.E. Sharp, J.M.J. Swanson, R.V. Farese, and T.C. Walther. 2020. Determinants of Endoplasmic Reticulum-to-Lipid Droplet Protein Targeting. *Dev. Cell.* 54:471-487.e7. doi:10.1016/j.devcel.2020.07.001.

Olzmann, J.A., and P. Carvalho. 2019. Dynamics and functions of lipid droplets. *Nat. Rev. Mol. Cell Biol.* 20:137–155. doi:10.1038/s41580-018-0085-z.

Olzmann, J.A., C.M. Richter, and R.R. Kopito. 2013. Spatial regulation of UBXD8 and p97/VCP controls ATGL-mediated lipid droplet turnover. *Proc. Natl. Acad. Sci.* 110:1345–1350. doi:10.1073/pnas.1213738110.

Parrinello, M., and A. Rahman. 1981. Polymorphic transitions in single crystals: A new molecular dynamics method. *J. Appl. Phys.* 52:7182–7190. doi:10.1063/1.328693.

Pataki, C.I., J. Rodrigues, L. Zhang, J. Qian, B. Efron, T. Hastie, J.E. Elias, M. Levitt, and R.R. Kopito. 2018. Proteomic analysis of monolayer-integrated proteins on lipid droplets identifies amphipathic interfacial α-helical membrane anchors. *Proc. Natl. Acad. Sci.* 115. doi:10.1073/pnas.1807981115.

Prévost, C., M.E. Sharp, N. Kory, Q. Lin, G.A. Voth, R.V. Farese, and T.C. Walther. 2018. Mechanism and Determinants of Amphipathic Helix-Containing Protein Targeting to Lipid Droplets. *Dev. Cell.* 44:73-86.e4. doi:10.1016/j.devcel.2017.12.011.

Ren, J., C. Pei-Chen Lin, M.C. Pathak, B.R.S. Temple, A.H. Nile, C.J. Mousley, M.C. Duncan, D.M. Eckert, T.J. Leiker, P.T. Ivanova, D.S. Myers, R.C. Murphy, H.A. Brown, J. Verdaasdonk, K.S. Bloom, E.A. Ortlund, A.M. Neiman, and V.A. Bankaitis. 2014. A phosphatidylinositol transfer protein integrates phosphoinositide signaling with lipid droplet metabolism to regulate a developmental program of nutrient stress–induced membrane biogenesis. *Mol. Biol. Cell.* 25:712–727. doi:10.1091/mbc.e13-11-0634.

Renne, M.F., R.A. Corey, J.V. Ferreira, P.J. Stansfeld, and P. Carvalho. 2022. Seipin concentrates distinct neutral lipids via interactions with their acyl chain carboxyl esters. *J. Cell Biol.* 221:e202112068. doi:10.1083/jcb.202112068.

Rogers, S., L. Gui, A. Kovalenko, V. Zoni, M. Carpentier, K. Ramji, K. Ben Mbarek, A. Bacle, P. Fuchs, P. Campomanes, E. Reetz, N.O. Speer, E. Reynolds, A.R. Thiam, S. Vanni, D. Nicastro, and W.M. Henne. 2022. Triglyceride lipolysis triggers liquid crystalline phases in lipid droplets and alters the LD proteome. *J. Cell Biol.* 221:e202205053. doi:10.1083/jcb.202205053.

Rowe, E.R., M.L. Mimmack, A.D. Barbosa, A. Haider, I. Isaac, M.M. Ouberai, A.R. Thiam, S. Patel, V. Saudek, S. Siniossoglou, and D.B. Savage. 2016. Conserved Amphipathic Helices Mediate Lipid Droplet Targeting of Perilipins 1–3. *J. Biol. Chem.* 291:6664–6678. doi:10.1074/jbc.M115.691048.

Sandager, L., M.H. Gustavsson, U. Ståhl, A. Dahlqvist, E. Wiberg, A. Banas, M. Lenman, H. Ronne, and S. Stymne. 2002. Storage Lipid Synthesis Is Non-essential in Yeast. *J. Biol. Chem.* 277:6478–6482. doi:10.1074/jbc.M109109200.

Schmeisser, S., S. Li, B. Bouchard, M. Ruiz, C. Des Rosiers, and R. Roy. 2019. Muscle-Specific Lipid Hydrolysis Prolongs Lifespan through Global Lipidomic Remodeling. *Cell Rep.* 29:4540-4552.e8. doi:10.1016/j.celrep.2019.11.090.

Schmidt, C., K. Athenstaedt, B. Koch, B. Ploier, and G. Daum. 2013. Regulation of the Yeast Triacylglycerol Lipase Tgl3p by Formation of Nonpolar Lipids. *J. Biol. Chem.* 288:19939–19948. doi:10.1074/jbc.M113.459610.

Schmidt, C., K. Athenstaedt, B. Koch, B. Ploier, M. Korber, G. Zellnig, and G. Daum. 2014. Defects in triacylglycerol lipolysis affect synthesis of triacylglycerols and steryl esters in the yeast. *Biochim. Biophys. Acta BBA - Mol. Cell Biol. Lipids*. 1841:1393–1402. doi:10.1016/j.bbalip.2014.07.001.

Schott, M.B., S.G. Weller, R.J. Schulze, E.W. Krueger, K. Drizyte-Miller, C.A. Casey, and M.A. McNiven. 2019. Lipid droplet size directs lipolysis and lipophagy catabolism in hepatocytes. *J. Cell Biol.* 218:3320–3335. doi:10.1083/jcb.201803153.

Shaw, D.E., J.P. Grossman, J.A. Bank, B. Batson, J.A. Butts, J.C. Chao, M.M. Deneroff, R.O. Dror, A. Even, C.H. Fenton, A. Forte, J. Gagliardo, G. Gill, B. Greskamp, C.R. Ho, D.J. Ierardi, L. Iserovich, J.S. Kuskin, R.H. Larson, T. Layman, L.-S. Lee, A.K. Lerer, C. Li, D. Killebrew, K.M. Mackenzie, S.Y.-H. Mok, M.A. Moraes, R. Mueller, L.J. Nociolo, J.L. Peticolas, T. Quan, D. Ramot, J.K. Salmon, D.P. Scarpazza, U.B. Schafer, N. Siddique, C.W. Snyder, J. Spengler, P.T.P. Tang, M. Theobald, H. Toma, B. Towles, B. Vitale, S.C. Wang, and C. Young. 2014. Anton 2: Raising the Bar for Performance and Programmability in a Special-Purpose Molecular Dynamics Supercomputer. *In* SC14: International Conference for High Performance Computing, Networking, Storage and Analysis. IEEE, New Orleans, LA, USA. 41–53.

Sorger, D., K. Athenstaedt, C. Hrastnik, and G. Daum. 2004. A Yeast Strain Lacking Lipid Particles Bears a Defect in Ergosterol Formation. *J. Biol. Chem.* 279:31190–31196. doi:10.1074/jbc.M403251200.

Strande, S., H. Cai, M. Tatineni, W. Pfeiffer, C. Irving, A. Majumdar, D. Mishin, R. Sinkovits, M. Norman, N. Wolter, T. Cooper, I. Altintas, M. Kandes, I. Perez, M. Shantharam, M. Thomas, S. Sivagnanam, and T. Hutton. 2021. Expanse: Computing without Boundaries: Architecture, Deployment, and Early Operations Experiences of

a Supercomputer Designed for the Rapid Evolution in Science and Engineering. *In* Practice and Experience in Advanced Research Computing. ACM, Boston MA USA. 1–4.

Sui, X., H. Arlt, K.P. Brock, Z.W. Lai, F. DiMaio, D.S. Marks, M. Liao, R.V. Farese, and T.C. Walther. 2018. Cryo–electron microscopy structure of the lipid droplet–formation protein seipin. *J. Cell Biol.* 217:4080–4091. doi:10.1083/jcb.201809067.

Sztalryd, C., and D.L. Brasaemle. 2017. The perilipin family of lipid droplet proteins: Gatekeepers of intracellular lipolysis. *Biochim. Biophys. Acta BBA - Mol. Cell Biol. Lipids*. 1862:1221–1232. doi:10.1016/j.bbalip.2017.07.009.

Szymanski, K.M., D. Binns, R. Bartz, N.V. Grishin, W.-P. Li, A.K. Agarwal, A. Garg, R.G.W. Anderson, and J.M. Goodman. 2007. The lipodystrophy protein seipin is found at endoplasmic reticulum lipid droplet junctions and is important for droplet morphology. *Proc. Natl. Acad. Sci.* 104:20890–20895. doi:10.1073/pnas.0704154104.

Teixeira, V., L. Johnsen, F. Martínez-Montañés, A. Grippa, L. Buxó, F.-Z. Idrissi, C.S. Ejsing, and P. Carvalho. 2018. Regulation of lipid droplets by metabolically controlled Ldo isoforms. *J. Cell Biol.* 217:127–138. doi:10.1083/jcb.201704115.

Thiam, A.R., and M. Beller. 2017. The why, when and how of lipid droplet diversity. *J. Cell Sci.* jcs.192021. doi:10.1242/jcs.192021.

Thiam, A.R., and L. Forêt. 2016. The physics of lipid droplet nucleation, growth and budding. *Biochim. Biophys. Acta BBA - Mol. Cell Biol. Lipids*. 1861:715–722. doi:10.1016/j.bbalip.2016.04.018.

Tribello, G.A., M. Bonomi, D. Branduardi, C. Camilloni, and G. Bussi. 2014. PLUMED 2: New feathers for an old bird. *Comput. Phys. Commun.* 185:604–613. doi:10.1016/j.cpc.2013.09.018.

Tsirigos, K.D., C. Peters, N. Shu, L. Käll, and A. Elofsson. 2015. The TOPCONS web server for consensus prediction of membrane protein topology and signal peptides. *Nucleic Acids Res.* 43:W401–W407. doi:10.1093/nar/gkv485.

Ugrankar, R., J. Bowerman, H. Hariri, M. Chandra, K. Chen, M.-F. Bossanyi, S. Datta, S. Rogers, K.M. Eckert, G. Vale, A. Victoria, J. Fresquez, J.G. McDonald, S. Jean, B.M. Collins, and W.M. Henne. 2019. Drosophila Snazarus Regulates a Lipid Droplet Population at Plasma Membrane-Droplet Contacts in Adipocytes. *Dev. Cell*. 50:557-572.e5. doi:10.1016/j.devcel.2019.07.021.

Valm, A.M., S. Cohen, W.R. Legant, J. Melunis, U. Hershberg, E. Wait, A.R. Cohen, M.W. Davidson, E. Betzig, and J. Lippincott-Schwartz. 2017. Applying systems-level

spectral imaging and analysis to reveal the organelle interactome. *Nature*. 546:162–167. doi:10.1038/nature22369.

Vaughan, M., J.E. Berger, and D. Steinberg. 1964. Hormone-sensitive Lipase and Monoglyceride Lipase Activities in Adipose Tissue. *J. Biol. Chem.* 239:401–409. doi:10.1016/S0021-9258(18)51692-6.

Velázquez, A.P., T. Tatsuta, R. Ghillebert, I. Drescher, and M. Graef. 2016. Lipid droplet–mediated ER homeostasis regulates autophagy and cell survival during starvation. *J. Cell Biol.* 212:621–631. doi:10.1083/jcb.201508102.

Walther, T.C., J. Chung, and R.V. Farese. 2017. Lipid Droplet Biogenesis. *Annu. Rev. Cell Dev. Biol.* 33:491–510. doi:10.1146/annurev-cellbio-100616-060608.

Wang, C.-W., Y.-H. Miao, and Y.-S. Chang. 2014. Size control of lipid droplets in budding yeast requires a collaboration of Fld1 and Ldb16. *J. Cell Sci.* jcs.137737. doi:10.1242/jcs.137737.

Wang, H., M. Becuwe, B.E. Housden, C. Chitraju, A.J. Porras, M.M. Graham, X.N. Liu, A.R. Thiam, D.B. Savage, A.K. Agarwal, A. Garg, M.-J. Olarte, Q. Lin, F. Fröhlich, H.K. Hannibal-Bach, S. Upadhyayula, N. Perrimon, T. Kirchhausen, C.S. Ejsing, T.C. Walther, and R.V. Farese. 2016. Seipin is required for converting nascent to mature lipid droplets. *eLife*. 5:e16582. doi:10.7554/eLife.16582.

Welte, M.A. 2015. Expanding Roles for Lipid Droplets. *Curr. Biol.* 25:R470–R481. doi:10.1016/j.cub.2015.04.004.

Wilfling, F., H. Wang, J.T. Haas, N. Krahmer, T.J. Gould, A. Uchida, J.-X. Cheng, M. Graham, R. Christiano, F. Fröhlich, X. Liu, K.K. Buhman, R.A. Coleman, J. Bewersdorf, R.V. Farese, and T.C. Walther. 2013. Triacylglycerol Synthesis Enzymes Mediate Lipid Droplet Growth by Relocalizing from the ER to Lipid Droplets. *Dev. Cell*. 24:384–399. doi:10.1016/j.devcel.2013.01.013.

Wolinski, H., H.F. Hofbauer, K. Hellauer, A. Cristobal-Sarramian, D. Kolb, M. Radulovic, O.L. Knittelfelder, G.N. Rechberger, and Sepp.D. Kohlwein. 2015. Seipin is involved in the regulation of phosphatidic acid metabolism at a subdomain of the nuclear envelope in yeast. *Biochim. Biophys. Acta BBA - Mol. Cell Biol. Lipids*. 1851:1450–1464. doi:10.1016/j.bbalip.2015.08.003.

Wright, R. 2000. Transmission electron microscopy of yeast. *Microsc. Res. Tech.* 51:496–510. doi:10.1002/1097-0029(20001215)51:6<496::AID-JEMT2>3.0.CO;2-9.

Yan, R., H. Qian, I. Lukmantara, M. Gao, X. Du, N. Yan, and H. Yang. 2018. Human SEIPIN Binds Anionic Phospholipids. *Dev. Cell*. 47:248-256.e4. doi:10.1016/j.devcel.2018.09.010.

Yang, X., X. Lu, M. Lombès, G.B. Rha, Y.-I. Chi, T.M. Guerin, E.J. Smart, and J. Liu. 2010. The G0/G1 Switch Gene 2 Regulates Adipose Lipolysis through Association with Adipose Triglyceride Lipase. *Cell Metab.* 11:194–205. doi:10.1016/j.cmet.2010.02.003.

Zechner, R., F. Madeo, and D. Kratky. 2017. Cytosolic lipolysis and lipophagy: two sides of the same coin. *Nat. Rev. Mol. Cell Biol.* 18:671–684. doi:10.1038/nrm.2017.76.

Zehmer, J.K., R. Bartz, B. Bisel, P. Liu, J. Seemann, and R.G.W. Anderson. 2009. Targeting sequences of UBXD8 and AAM-B reveal that the ER has a direct role in the emergence and regression of lipid droplets. *J. Cell Sci.* 122:3694–3702. doi:10.1242/jcs.054700.

Zhang, S., Y. Wang, L. Cui, Y. Deng, S. Xu, J. Yu, S. Cichello, G. Serrero, Y. Ying, and P. Liu. 2016. Morphologically and Functionally Distinct Lipid Droplet Subpopulations. *Sci. Rep.* 6:29539. doi:10.1038/srep29539.

Zhang, X., B.L. Heckmann, L.E. Campbell, and J. Liu. 2017. G0S2: A small giant controller of lipolysis and adipose-liver fatty acid flux. *Biochim. Biophys. Acta BBA - Mol. Cell Biol. Lipids*. 1862:1146–1154. doi:10.1016/j.bbalip.2017.06.007.

Zimmermann, R., J.G. Strauss, G. Haemmerle, G. Schoiswohl, R. Birner-Gruenberger, M. Riederer, A. Lass, G. Neuberger, F. Eisenhaber, A. Hermetter, and R. Zechner. 2004. Fat Mobilization in Adipose Tissue Is Promoted by Adipose Triglyceride Lipase. *Science*. 306:1383–1386. doi:10.1126/science.1100747.